JOURNAL OF GEOPHYSICAL RESEARCH, VOL. 102, NO. B6, PAGES 11,789-11,813, JUNE 10, 1997

Crust and upper mantle shear velocity structure beneath the Tibetan plateau and surrounding regions from interevent surface wave phase velocity inversion

Andrew Curtis[1] and John H. Woodhouse
Department of Earth Sciences, Oxford University, England

Abstract. Average a priori shear velocity models are constructed for the Tien Shan, Tarim basin, Pamir–Hindu Kush, Himalaya and NE India. These models are shown to account for most of the lateral velocity heterogeneity at wavelengths > 1000 km. Interevent fundamental mode Rayleigh and Love wave phase velocities were measured in the period range 32–200 s and were inverted for path-averaged shear velocity structures. These, in turn, were regionalized to estimate average, isotropic structures beneath the six regions listed above. Low upper mantle velocities are observed beneath the western and eastern Tien Shan. The Tarim basin structure is poorly constrained but exhibits very low upper crustal velocities (probably due to deep sedimentary accumulation), and either very high upper mantle velocities exist (> 4.8 km/s) in a layer 70 km thick or the lithosphere is very thick (~180 km). Low upper mantle velocities are observed beneath the Chang Thang region, the central, and the northeast plateau but not beneath the southern or southeastern plateau. The crustal velocity gradient with depth is zero in the east central plateau consistent with lower crustal basaltic intrusions there but is positive to the west and southeast of this zone. Upper mantle structures show that the Indian lithosphere could have subducted beneath the entire plateau only if either 1 mantle in the depth range 115–185 km has been altered (or removed) to reduce its average velocity or 2 the Indian lithosphere is only ~85 km thick.

Introduction

India collided with Asia in the Eocene around 40–50 Ma [*Fisher et al.*, 1971; *McKenzie and Sclater*, 1971; *Sahni and Kumar*, 1974; *Molnar and Tapponnier*, 1975]. Continued convergence has accommodated between 1800 and 2500 km of crustal shortening, creating crustal thicknesses of between 55 and 80 km over an area of 1.5×10^6 km^2 within the Tibetan plateau [*McKenzie and Sclater*, 1971; *Molnar and Tapponnier*, 1975; *Molnar*, 1984, 1988; *Holt and Wallace*, 1990; *Zhao and Xie*, 1993].

There are four main views on how this shortening has been accommodated: (1) Subduction of India along the main boundary thrust has underplated most, or the whole of the Tibetan plateau with the Indian shield; the buoyant shield material lifts the overlying Asian crust creating the plateau [*Barazangi and Ni*, 1982]. Certainly, there is evidence for underthrusting beneath the Himalaya from earthquake source mechanisms and locations [*Ni and Barazangi*, 1984; *Baranowski et al.*, 1984,] but this seismicity only extends approximately 150 km north of the subduction zone, so any more extensive underthrusting must be aseismic. (2) Diffuse thickening and extrusion of the entire Asian lithosphere create the plateau due to isostatic buoyancy forces [*Dewey and Burke*, 1973; *Molnar and Tapponnier*, 1975; *England and McKenzie*, 1982; *England and Houseman*, 1986; *Peltzer et al.*, 1988; *Armijo et al.*, 1989]. (3) Indian crustal material is injected into the "fluid" Asian lower crust; lower crustal flow is blocked by surrounding cratonic regions causing the plateau upper crust to be elevated pneumatically [*Zhao and Morgan*, 1985, 1987; *Westaway*, 1995]. (4) Diffuse accumulation and thickening of Asian crustal material stripped off subducted Asian lithosphere cause increased plateau elevation [*Willett and Beaumont*, 1994].

In regions of the world with high seismic activity, travel times of different modes and waveforms can place constraints on the velocity structure of the crust and mantle. In Tibet, however, the lack of seismic stations within or on the edges of the plateau decreases the possible resolution dramatically and introduces large ambiguities in structural interpretation of travel times. The lack of seismological constraints is especially acute be-

[1]Now at the Department of Theoretical Geophysics, Utrecht University, The Netherlands.

Paper number 96JB03182.
0148-0227/97/96JB-03182$09.00

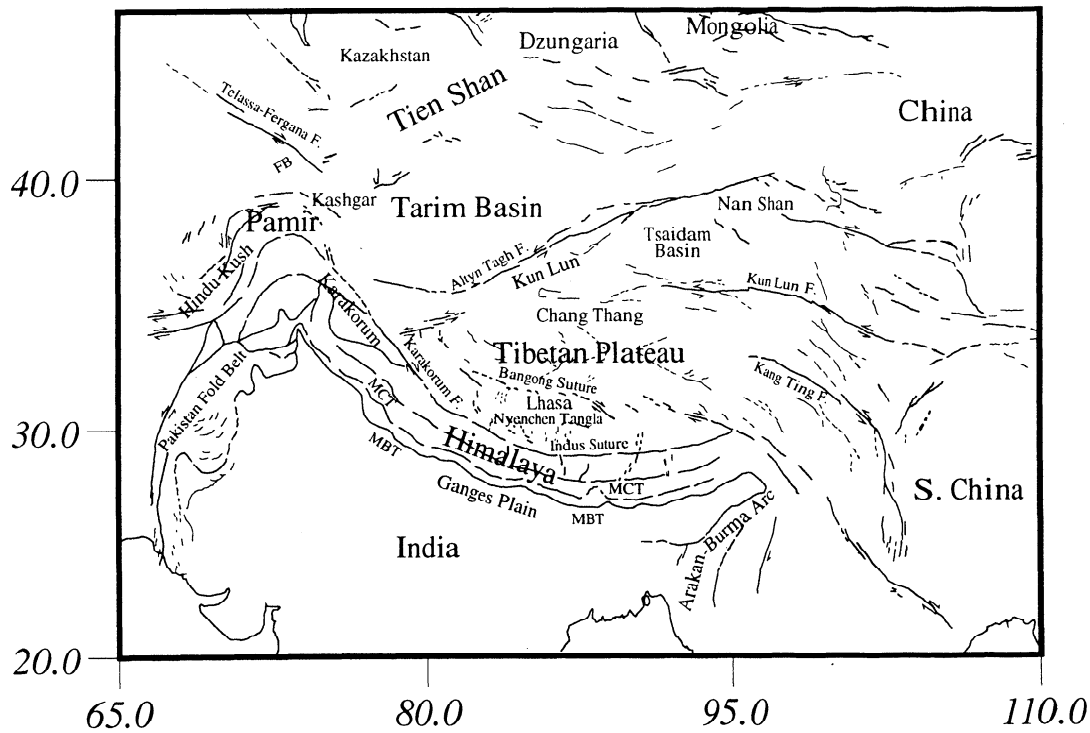

Figure 1. The Tibetan region, geographical names used in the text. Abbreviation are as follows: MBT, Main Boundary Thrust; MCT, Main Central Thrust; FB, Fergana basin.

neath the Tarim basin to the north of the plateau (see Table 3), and hence new constraints anywhere within the Tibetan region (Figure 1) may be invaluable to the understanding of subsurface mechanisms of lithospheric shortening.

In the current work we constrain the average isotropic crust and upper mantle shear velocity structure across the Tibetan region by phase velocity analysis and structural inversion of surface wave trains from earthquakes occurring in and around the plateau arriving at seismological stations world wide. To isolate that component of the signal due to structure within the Tibetan region, we use data only from pairs of events aligned with one station; the difference in event–station phase delays is attributed to the portion of paths between the two events [*Romanowicz*, 1982]. Without the installation of seismographs within the Tibetan region, this is the only method of obtaining pure path seismic velocity measurements. We measure and invert phase delays along 59 interevent paths across the Tibetan region. Average path structures are then regionalized to give the average structure in six geologically distinct provinces: the Tien Shan, Tarim basin, Pamir–Hindu Kush, Tibetan plateau, Himalaya, and Indian shield (Figure 1). Our interpretation is described in the discussion, and all results are summarized in the conclusions.

Data Selection and Methodology

We use the method of *Romanowicz* [1982] to measure interevent phase delays. As described above, this requires that paths from pairs of earthquakes to any single teleseismic station are aligned. Below we describe the data selection criterion, the process of signal filtration, and phase dispersion measurement; then the inversion procedures are described for both path and regional inversions.

Alignment Criterion and Signal Filtration

The International Seismological Centre (ISC) earthquake source catalogue and locations of all teleseismic long-period Global Digital Seismograph Network (GDSN) and Geoscope stations were searched for alignments of event–station paths. Surface waves sample laterally on a length scale proportional to their wavelength and within the 35–200 s period range considered here, their velocities will be affected by crustal properties within at least 100 km of the great circle path. Hence we impose a maximum allowable lateral distance of 50 km between each pair of event–station great circle paths. Using this search criterion, a network of 257 interevent path alignments was found.

For each recorded signal, the instrument response was deconvolved and replaced by an amplitude scaling factor $1/\omega$ (to boost amplitudes at longer periods) with no phase change over the interval 45 to 250 s, tapering to zero at either end to 32 s and 450 s, respectively. Only long-period vertical (LPZ) and transverse (LPT) components were used, recording Love and Rayleigh arrivals, respectively. Signals were decimated to a sampling interval of 16 s since all energy below a 32 s period was removed.

Signals were analyzed using moving window analysis

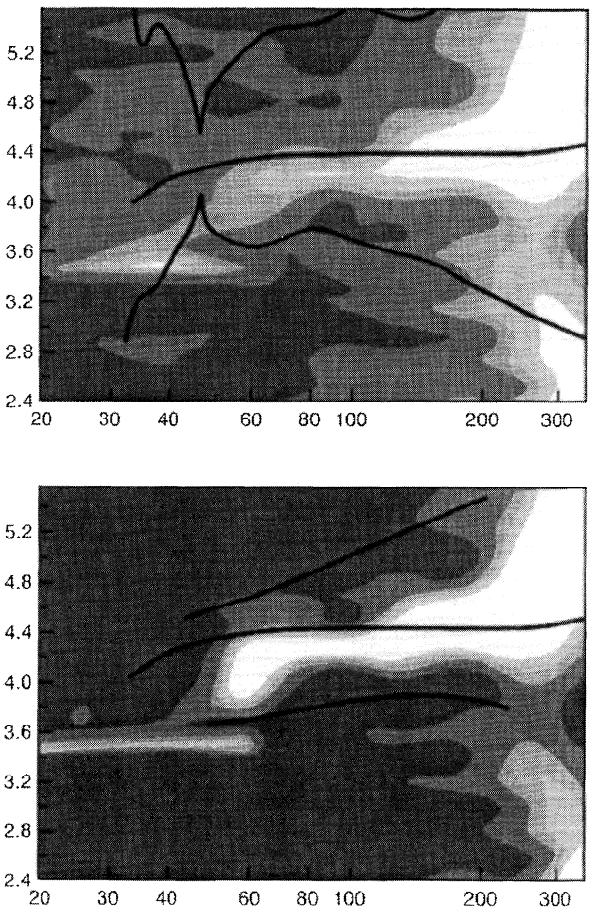

Figure 2. Examples of contoured energy on a velocity–period plot for the fundamental mode long-period transverse surface wave component of August 20, 1988, event recorded at station COL. (top) A nonnormalized energy grid with the group velocity dispersion curve of PREM [*Dziewonski and Anderson* 1981] shown as the central smooth solid line, flanked by the lines marking the boundary widths defined by the third order formulae of *Cara* [1973]. (bottom) The column-normalized grid for the same signal with hand-picked boundary widths.

[*Landisman et al.*, 1969]. Examples are shown in Figure 2 for the transverse signal component from event August 20, 1988, at station COL. Around each point in time the amplitude of frequency components within an interval of length $W \times T$ are contoured, where T is period and the value $W = 3.0$ was chosen empirically. The ridge of high amplitude clearly defines the fundamental mode group arrival, especially when columns are normalized to have the same maximum value (Figure 2, bottom), but also holes in the time–frequency spectrum and the arrival of other phases can be detected.

Time variable filtration allows filtered seismograms to be constructed from energy arriving around the main group arrival only [*Landisman et al.*, 1969]. Usually, energy is included within some temporal half width around the group velocity curve, for which *Cara* [1973] provides a theoretically optimal definition with respect to time and frequency resolution (see Figure 2, top). However, this method often includes noise from other unwanted arrivals in filtered signals. Instead, we picked upper and lower filter width boundaries $t_1(\omega)$ and $t_2(\omega)$ for every seismogram used (Figure 2, bottom). Time-frequency components were weighted with the function

$$B(t) = \begin{cases} 0 & t < t_1(\omega) \\ 1 - \left[\frac{t - \frac{1}{2}(t_2(\omega) - t_1(\omega))}{t_2(\omega) - t_1(\omega)}\right]^4 & t_1(\omega) \le t \le t_2(\omega) \\ 0 & t > t_2(\omega) \end{cases} \quad (1)$$

as used by Cara. Thus interference caused by other phase arrivals can be avoided, and it will be shown below that this method can be used to calculate variances of phase velocities. Figure 3 shows example recorded and synthetic data before and after filtering. Notice that phase is preserved in the portion of maximum amplitude, whereas noise elsewhere is removed.

Phase Velocities

Event–station phase velocities were found by cross-correlating filtered synthetic seismograms and data to obtain the phase delay spectrum, defining the integral cycle number by assuming continuity of phase from long periods to short. Synthetics were calculated for model PEM–C [*Dziewonski et al.*, 1975] using centroid moment tensor source solutions and depths [*Dziewonski and Woodhouse*, 1983] and ISC epicentral coordinates.

Interevent phase velocities were found using the method of *Romanowicz* [1982] and *Brandon and Romanowicz* [1986]. The phase of an arrival of frequency ω from event i at a station can be written

$$\Phi_i = -\frac{\omega X_i}{C_i} + \omega T_i + \Phi_i^s + \Phi_R + 2\pi N_i \quad (2)$$

where Φ_R is the instrumental phase, X_i is the epicentral distance, C_i is the average phase velocity on the source station path, Φ_i^s is the source phase, T_i is the time of the beginning of the data window with respect to origin time of event i, and N_i is the number of cycles. The phase difference between two such events ($i = 1, 2$) is

$$\begin{aligned} \Delta\Phi &= \Phi_2 - \Phi_1 \\ &= \frac{\omega X_1}{C_1} - \frac{\omega X_2}{C_2} + \Phi_2^s - \Phi_1^s + 2\pi(N_2 - N_1) \\ &\quad + \omega(T_2 - T_1) \end{aligned} \quad (3)$$

and if we assume that the paths are well enough aligned and a sufficient distance apart to justify phase additivity, then we can use the formula

$$\frac{\omega X}{C} = \frac{\omega X_1}{C_1} - \frac{\omega X_2}{C_2} \quad (4)$$

to estimate the interevent average phase velocity C, where X is the interevent distance.

The network of paths for which data quality was sufficient to pass filtration and phase velocity determination is shown in Figure 4. These are tabulated in Table 1 for events listed in Table 2.

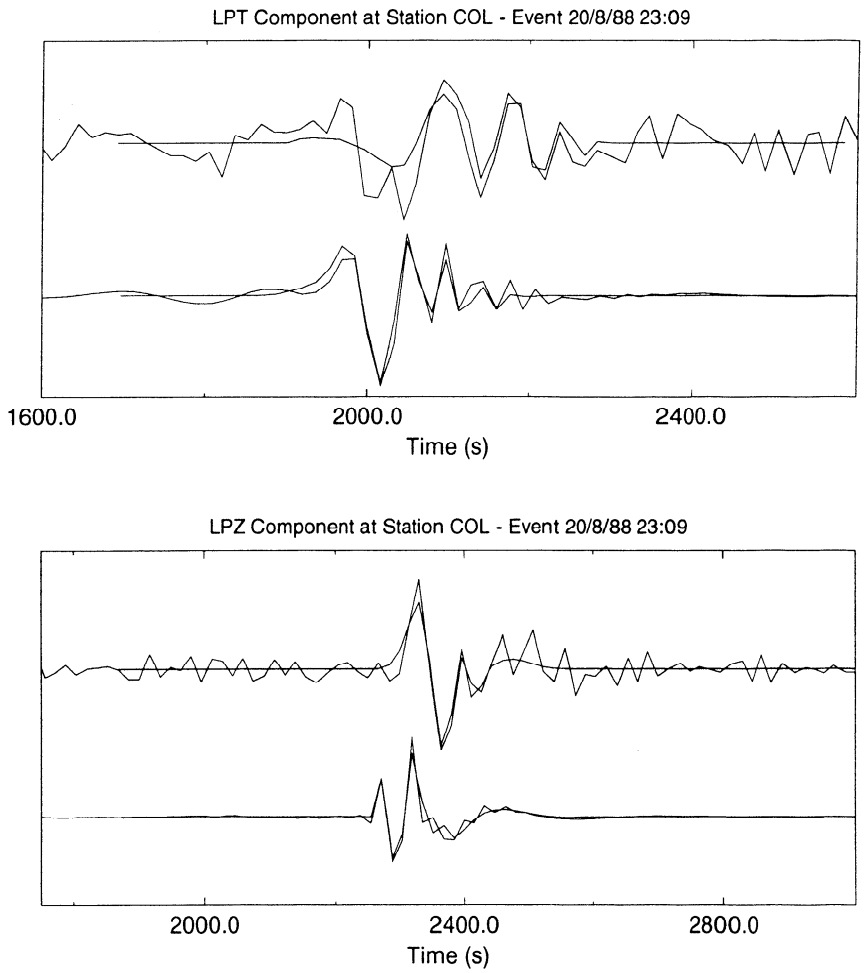

Figure 3. Original and filtered data and fundamental mode synthetics for August 20, 1988, event recorded at station COL, decimated to 16 s sampling interval. (top) The transverse (LPT) component; (bottom) the vertical (LPZ) component. In each graph, the top traces are recorded and filtered data, while the bottom traces are the original and filtered synthetic. In all cases, filtered signals are smoother and die away to zero more rapidly than the original data. The horizontal axis is time after the event median source time; the vertical axis is a nondimensionalized measure of displacement.

Variance of Phase Velocity Measurements

For each pair of events aligned with one station, the process of time-variable filtration and interevent phase velocity calculation was carried out five times. Each time, a different band of energy in time–frequency space was picked to be included in filtered signals and synthetics. Each band included the main group arrival but had variable width while still avoiding all other prominent arrivals. Hence the only difference between the five reconstructed filtered signals was that each contained a different portion of background noise (visible in Figure 2, top). This process gave five independent estimates of phase velocity as a function of frequency, $c_i(w)$, $i = 1, \cdots, 5$. Differences between the five results are due to different selections of the dispersion bands alone and are a measure of the precision of the resulting phase velocities.

The mean phase velocity curve $c(\omega)$ and the frequency dependent variance relationship $\sigma^2(\omega)$ were calculated for each path. Examples of relations $c_i(\omega)$, $c(\omega)$ and $\sigma(\omega)$ are shown in Figure 5 for the path pl03a in Figure 4. Notice the divergence of phase velocity curves and the corresponding increase in σ at long periods. This indicates that the mean phase velocity estimate at long periods is much less reliable than at short periods.

In previous studies, a constant measurement variance has been assumed for phase velocities. The automatic signal filtration used in most of these will not be best suited to each measured signal, and phase velocities will be correspondingly less precisely measured. Unless some other information is available, a better estimate of measurement precision of event–station phase velocities for future studies is half the average interevent path measurement variance over Tibet, as calculated

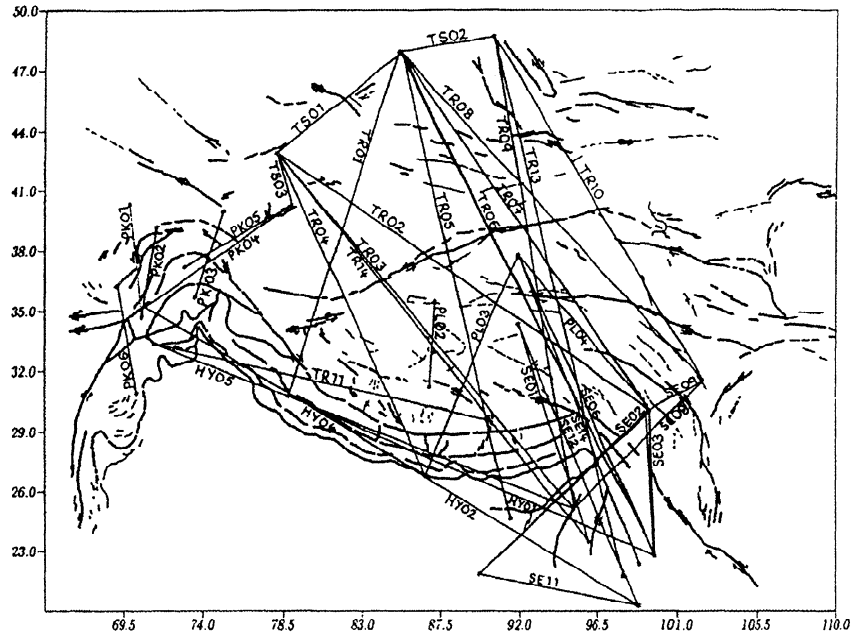

Figure 4. The network of paths which ultimately had data of sufficient quality to be used throughout the current study. These are tabulated in Table 1.

from the present results. Corresponding average standard deviations found in the present study are shown in Figure 6.

Phase velocity measurement precision such as that shown in Figures 5 and 6 does not include errors due to uncertainty in the location and mechanism of the seismic source. Each interevent phase velocity measurement is dependent on two seismic source estimates. Relative errors between the two source phases perturb phase velocity measurements in inverse proportion to path length. Two paths in this study are only approximately 300 km long; a relative source location error of 30 km on these paths could cause an error in phase velocity of up to 10%. However, on average our paths are around 1200 km long, and for such paths, a similar source error would translate to a phase velocity error of around 2.5%. In addition, since we expect source location bias to be laterally systematic due to the geometry of global station coverage, relative location errors for each source pair should be lower for short paths than for longer ones.

Uncertainties due to source depth or mechanism errors are more difficult to quantify, but again these effects will be inversely proportional to path length. An additional uncertainty arises because deviations from the great circle may be significant on the longer paths. In summary then, source errors may bias our results mainly on the short paths, while off-great circle path propagation may be significant on longer paths.

Inversion for Average Velocity Structure Along a Path

An iterated linear weighted least squares procedure was used to invert interevent phase velocity dispersion curves for velocity structure [*Tarantola and Valette*, 1982]. Let the data vector $\mathbf{d}$ comprise interevent phase delay measurements at a range of frequencies along any path and the model vector $\mathbf{x}$ comprise average model parameters along the path. We invert for Moho depth plus two crustal and two mantle velocity layers; hence $\mathbf{x}$ has five elements for each path. We represent the forward theory of estimating $\mathbf{d}$ given $\mathbf{x}$ by the function $\mathbf{G}(\mathbf{x})$. Let $\rho_{\mathbf{p}}(\mathbf{x})$ be the probability distribution representing all a priori parameter information. This will be constructed below, but we assume here that $\rho_{\mathbf{p}}(\mathbf{x})$ is Gaussian with mean $\mathbf{x}_0$ and variance $\mathbf{S}^2$. Hence

$$\rho_{\mathbf{p}}(\mathbf{x}) \propto \exp\ \left(-\tfrac{1}{2}(\mathbf{x}-\mathbf{x}_0)^T C_0^{-1}(\mathbf{x}-\mathbf{x}_0)\right) \qquad (5)$$

where C_0 is the prior covariance matrix $\mathrm{diag}[\mathbf{S}_1^2, \ldots, \mathbf{S}_5^2]$.

The prior data information $\rho_{\mathbf{d}}(\mathbf{x})$ contains parameter information from phase velocity estimates plus their Gaussian measurement uncertainties:

$$\rho_{\mathbf{d}}(\mathbf{x}) \propto \exp\ \left\{-\tfrac{1}{2}[G(\mathbf{x})-\mathbf{d}]^T C_{\mathbf{d}}^{-1}[G(\mathbf{x})-\mathbf{d}]\right\} \qquad (6)$$

The diagonal matrix $C_{\mathbf{d}}$ describes measured data variances.

The a posteriori joint distribution is given by the product of equations (5) and (6) [*Tarantola and Valette*, 1982]:

$$\sigma(\mathbf{x}) \propto \exp\left\{ \begin{array}{c} -\tfrac{1}{2}[(G(\mathbf{x})-\mathbf{d})^T C_{\mathbf{d}}^{-1}(G(\mathbf{x})-\mathbf{d}) \\ +(\mathbf{x}-\mathbf{x}_0)^T C_0^{-1}(\mathbf{x}-\mathbf{x}_0)] \end{array} \right\} \qquad (7)$$

Since the sum of two quadratic forms is itself quadratic, $\sigma(\mathbf{x})$ is also Gaussian.

Let $\Psi(\mathbf{x})$ be the exponent in (7). The minimum misfit solution is found by solving

Table 1. Interevent Paths Used in the Current Study.

Path	Date A	Time A, UT	Date B	Time B, UT	Station	Distance, km	Length, km
pk01	Feb. 1, 1984	1422:07.7	Oct. 13, 1985	1559:53.5	RSON	9792.2	627.2
pk02	Feb. 1, 1984	1422:07.7	Oct. 26, 1984	2022:22.0	RSNT	8737.1	502.1
pk03	Sept. 12, 1981	0715:54.0	Feb. 13, 1983	0140:13.2	JAS	11246.4	497.4
pk04	Oct. 25, 1990	0453:46.5	Feb. 25, 1991	1430:29.3	KIP	10994.0	920.1
pk05	May 10, 1992	0404:32.8	Feb. 25, 1991	1430:29.3	HIA	3333.3	627.9
pk06	May 6, 1985	0304:22.3	Dec. 16, 1982	0040:48.6	RSON	10225.5	603.9
pl01	Oct. 19, 1991	2123:15.5	Jan. 14, 1990	0303:19.8	KIP	10213.1	1434.4
pl02	May 20, 1985	1511:40.4	June 20, 1986	1712:46.5	RSON	10458.9	469.3
pl03a	Aug. 20, 1988	2309:11.2	Jan. 14, 1990	0303:19.8	COL	7517.2	1315.4
pl03b	Aug. 20, 1988	2309:11.2	Jan. 14, 1990	0303:19.8	LON	10074.6	1315.1
pl03c	Aug. 20, 1988	2309:11.2	Jan. 14, 1990	0303:19.8	CMB	10998.2	1314.9
pl04a	Jan. 14, 1990	0303:19.8	May 3, 1989	0553:00.4	KMI	635.3	1102.1
pl04b	Jan. 14, 1990	0303:19.8	May 3, 1989	1541:31.3	KMI	632.9	1104.5
pl04c	Jan. 14, 1990	0303:19.8	April 15, 1989	2023:11.7	KMI	639.3	1098.6
pl04d	Jan. 14, 1990	0303:19.8	April 25, 1989	0213:24.6	KMI	634.0	1105.4
tr01b	Oct. 19, 1991	2123:15.5	Aug. 3, 1990	0915:04.1	LON	9210.5	1982.0
tr02a	Nov. 12, 1990	1228:49.0	April 25, 1989	0213:24.6	CTAO	7470.1	2379.0
tr02b	Nov. 12, 1990	1228:49.0	May 3, 1989	0553:00.4	CTAO	7470.2	2378.9
tr02c	Nov. 12, 1990	1228:49.0	May 3, 1989	1541:31.3	CTAO	7468.0	2381.1
tr04	Nov. 12, 1990	1228:49.0	Aug. 20, 1988	2309:11.2	KEV	4132.2	1952.4
tr05	July 30, 1992	0824:49.2	June 14, 1990	1247:28.3	SCP	10053.9	2077.3
tr06a	Nov. 30, 1988	0813:29.1	Aug. 3, 1990	0915:04.1	KEV	3902.6	3093.3
tr06b	Nov. 30, 1988	0813:29.1	June 14, 1990	1247:28.3	KEV	3914.5	3081.5
tr07a	June 14, 1990	1247:28.3	May 3, 1989	0553:00.4	KMI	635.3	2328.1
tr07e	June 14, 1990	1247:28.3	April 25, 1989	0213:24.6	KMI	634.0	2329.4
tr09	July 23, 1988	0738:09.9	Aug. 6, 1988	0036:24.6	GAC	9470.3	2647.8
tr08	June 14, 1990	1247:28.3	Sept. 22, 1989	0225:53.5	ESK	5762.4	2334.3
tr10	July 23, 1988	0738:09.9	Sept. 22, 1989	0225:53.5	KEV	4043.4	2156.0
tr11	May 20, 1992	1220:35.0	July 30, 1992	0824:49.2	KMI	1337.0	1840.1
tr13	March 1, 1989	0325:07.8	July 23, 1988	0738:09.9	GDH	6605.0	3066.1
se01a	Nov. 5, 1988	0214:30.8	Jan. 5, 1991	1457:11.5	WMQ	1115.0	1265.2
se02b	June 12, 1989	0004:10.4	April 15, 1989	2034:11.7	MDJ	3116.4	1305.3
se02e	June 12, 1989	0004:10.4	May 3, 1989	0553:00.4	BJI	1877.0	1329.7
se02h	June 12, 1989	0004:10.4	May 3, 1989	1541:31.3	MDJ	3092.9	1328.8
se03e	April 15, 1989	2034:11.7	Nov. 6, 1988	1303:17.1	GAC	11622.6	795.8
se03g	April 25, 1989	0213:24.6	Nov. 6, 1988	1303:17.1	SCP	12173.5	801.3
se03h	Nov. 30, 1988	0813:29.1	April 25, 1989	0213:24.6	SCP	12173.5	808.2
se03i	Nov. 6, 1988	1303:17.1	May 3, 1989	0553:00.4	SCP	12170.3	804.5
se03j	Nov. 30, 1988	0813:29.1	May 3, 1989	0553:00.4	SCP	12170.3	811.4
se03k	Nov. 6, 1988	1303:17.1	May 3, 1989	1541:31.3	SCP	12172.6	802.3
se03l	Nov. 30, 1988	0813:29.1	May 3, 1989	1541:31.3	SCP	12172.6	809.1
se04	Jan. 5, 1991	1457:11.5	April 25, 1989	0213:24.6	LON	10559.9	804.1
se06a	Jan. 14, 1990	0303:19.8	Nov. 30, 1988	0813:29.1	WMQ	759.5	1830.0
se06b	Jan. 14, 1990	0303:19.8	Nov. 6, 1988	1303:17.1	WMQ	759.5	1821.1
se08	Sept. 22, 1989	0225:53.5	Aug. 6, 1988	0036:24.6	RER	6654.2	1010.2
se09b	Sept. 22, 1989	0225:53.5	April 25, 1989	0213:24.6	SLR	9769.4	333.1
se11	June 12, 1989	0004:10.4	Sept. 30, 1989	1819:23.9	AFI	10468.5	958.9
se12b	Sept. 28, 1989	2152:17.0	Nov. 5, 1988	0214:30.8	KEV	5512.4	1695.5
se14a	Jan. 14, 1990	0303:19.8	April 23, 1992	1532:52.4	WMQ	759.5	1832.9
se14b	Jan. 14, 1990	0303:19.8	April 23, 1992	1418:37.9	WMQ	759.5	1834.6
ts01	Nov. 12, 1990	1228:49.0	June 14, 1990	1247:28.3	SLR	9148.5	778.3
ts02	Aug. 3, 1990	0915:04.1	July 23, 1988	0738:09.9	HIA	2128.5	420.0
ts03a	Feb. 25, 1991	1430:29.3	Nov. 12, 1990	1228:49.0	CCM	10986.3	297.4
hy01a	Aug. 6, 1988	0036:24.6	Oct. 19, 1991	2123:15.5	ZOBO	16297.0	1719.6
hy01b	Nov. 30, 1988	0813:29.1	Oct. 19, 1991	2123:15.5	ZOBO	16297.0	2267.5
hy02	Oct. 25, 1990	0453:46.5	Sept. 28, 1989	2152:17.0	CTAO	6828.3	3200.3
hy03	Feb. 6, 1988	1450:42.7	July 30, 1992	0824:49.2	WMQ	1594.6	560.3
hy04	Oct. 25, 1990	0453:46.5	Aug. 20, 1988	2309:11.2	TOL	6435.5	1775.3
hy05	Aug. 6, 1988	0036:24.6	May 20, 1992	1220:35.0	ZOBO	15535.1	2481.5

Columns are path name used in Figure 4, date and time of events A and B as shown in Table 2, station name, epicentral distance of the event nearest to the station and the interevent path length.

Table 2. Events Used in the Current Study

Date	Time, UT	Dt, s	Latitude	Longitude
July 23, 1988	0738:09.9	5.1	48.72	90.51
Aug. 6, 1988	0036:24.6	13.0	25.14	95.12
Aug. 20, 1988	2309:11.2	4.7	26.78	86.61
Jan. 14, 1990	0303:19.8	11.1	37.77	91.89
Feb. 1, 1984	1422:07.7	2.7	34.68	70.54
Oct. 13, 1985	1559:53.5	3.0	40.32	69.84
Oct. 26, 1984	2022:22.0	2.0	39.18	71.34
Sept. 12, 1981	0715:54.0	4.0	35.67	73.55
Feb. 13, 1983	0140:13.2	4.0	39.99	75.10
Oct. 25, 1990	0453:46.5	18.6	35.19	70.74
Feb. 25, 1991	1430:29.3	5.3	40.33	78.95
May 6, 1985	0304:22.3	6.2	30.88	70.25
Dec. 16, 1982	0040:48.6	5.9	36.24	69.10
May 20, 1985	1511:40.4	6.1	35.45	87.18
June 20, 1986	1712:46.5	5.2	31.22	86.86
May 3, 1989	0553:00.4	11.8	30.07	99.48
May 3, 1989	1541:31.3	9.2	30.05	99.49
Oct. 19, 1991	2123:15.5	6.1	30.74	78.79
Aug. 3, 1990	0915:04.1	8.4	47.95	84.96
Nov 12, 1990	1228:49.0	9.6	42.94	78.08
April 25, 1989	0213:24.6	6.6	30.04	99.45
July 30, 1992	0824:49.2	11.2	29.59	90.17
June 14, 1990	1247:28.3	4.3	47.89	85.12
Nov. 30, 1988	0813:29.1	-0.2	22.75	99.84
Sept. 22, 1989	0225:53.5	3.3	31.55	102.46
May 20, 1992	1220:35.0	0.1	33.32	71.27
March 1, 1989	0325:07.8	2.8	21.73	97.94
Feb. 6, 1988	1450:42.7	0.9	24.65	91.52
Nov. 5, 1988	0214:30.8	9.3	34.32	91.88
Jan. 5, 1991	1457:11.5	12.9	23.48	95.98
June 12, 1989	0004:10.4	5.9	21.86	89.77
April 15, 1989	2034:11.7	9.5	29.98	99.24
Nov. 6, 1988	1303:17.1	14.1	22.81	99.77
Sept. 30, 1989	1819:23.9	34.1	20.27	98.85
Sept. 28, 1989	2152:17.0	4.3	20.29	98.77
April 23, 1992	1532:52.4	1.6	22.36	98.86
April 23, 1992	1418:37.9	3.0	22.34	98.85
May 10, 1992	0404:32.8	1.1	37.19	72.94

Dt is source half-duration.

$$\frac{\partial}{\partial \mathbf{x}}\Psi(\mathbf{x}) = 0$$

$$\Rightarrow A^T(\mathbf{x})C_{\mathbf{d}}^{-1}(G(\mathbf{x}) - \mathbf{d}) + C_0^{-1}(\mathbf{x} - \mathbf{x_0}) = 0 \quad (8)$$

where

$$A(\mathbf{x}) = \frac{\partial G(\mathbf{x})}{\partial \mathbf{x}} \quad (9)$$

Equation (8) can be solved iteratively with the scheme

$$\mathbf{x}_{k+1} = \mathbf{x}_k + (A_k^T C_{\mathbf{d}}^{-1} A_k + C_0^{-1})^{-1} \times \left\{ \begin{array}{c} A_k^T C_{\mathbf{d}}^{-1}[\mathbf{d} - G(\mathbf{x}_k)] \\ -C_0^{-1}(\mathbf{x}_k - \mathbf{x}_0) \end{array} \right\} \quad (10)$$

easily verified by substitution. To find the posteriori covariance matrix C_p, we substitute the Taylor approximation $G(\mathbf{x}) \approx G(\mathbf{x}_m) + A(\mathbf{x}_m)(\mathbf{x} - \mathbf{x}_m)$ into $\Psi(\mathbf{x})$; the quadratic terms in $(\mathbf{x} - \mathbf{x}_m)$ give

$$C_p^{-1} = A^T(\mathbf{x}_m)C_{\mathbf{d}}^{-1}A(\mathbf{x}_m) + C_0^{-1} \quad (11)$$

Equations (10) and (11) perform one linear inversion of the data **d** for velocity structure **x**. Five successive inversions were carried out to account for nonlinearity in the forward model.

Inversion for Regionally Averaged Velocity Structure

Models of average velocity structure beneath paths crossing more than one region are difficult to interpret. Hence we inverted (or regionalized) interevent path-averaged structures for the average structure beneath each of the six regions defined in Figure 7.

The inversion technique was identical to that described in the previous section. Now, however, the model parameters **x** are the crustal thickness and shear velocities in four layer models for structure in each of the six regions, 30 parameters in all. The data **d** are the five-parameter velocity models found for each of

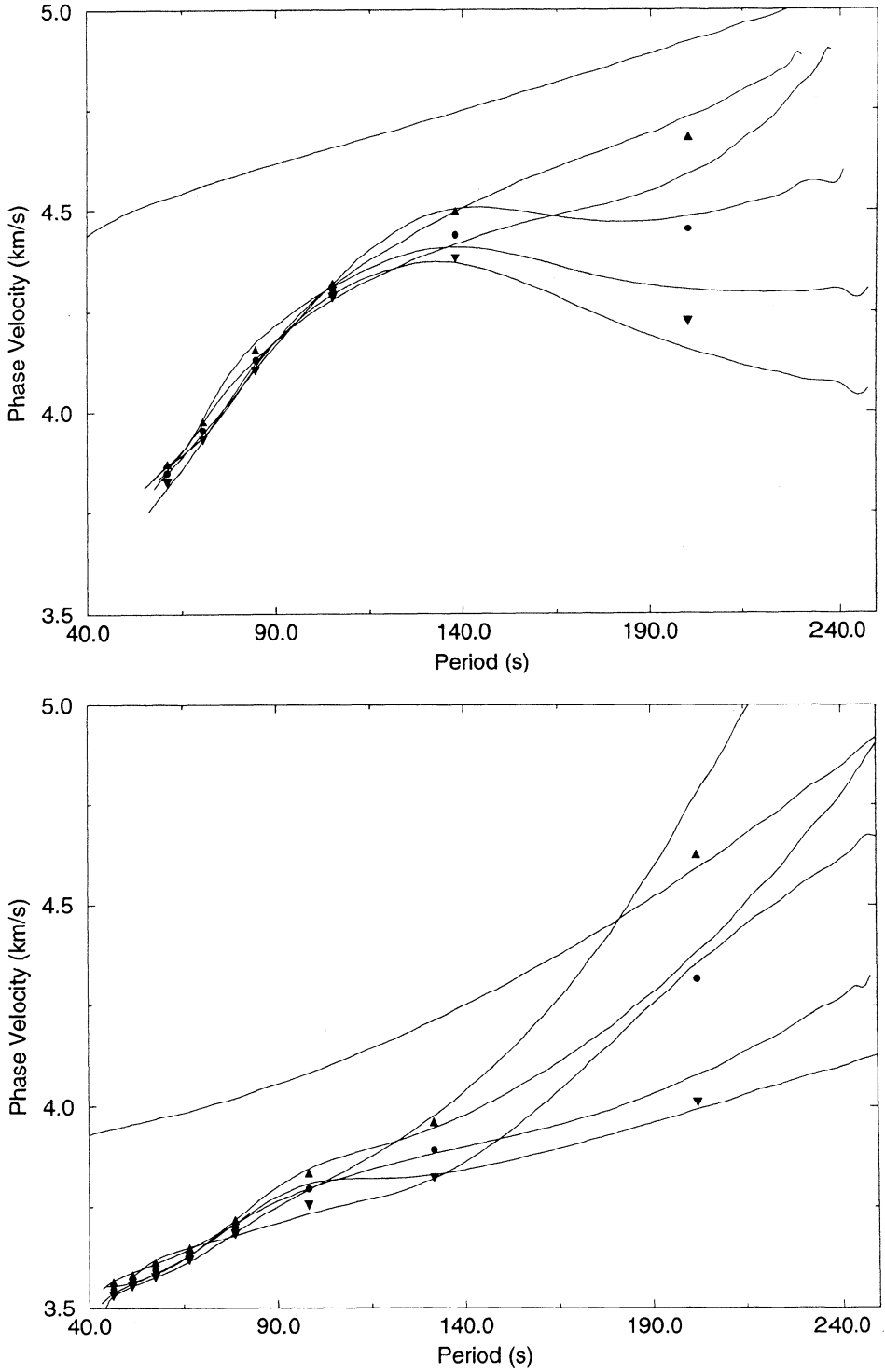

Figure 5. Phase velocities measured by the methods presented in the text along path pl03a shown in Figure 4. (top) Love wave velocities; (bottom) Rayleigh wave velocities. The smooth line in each plot which stands out from the rest is the phase velocity of model PREM for reference. There are five independent estimates of phase velocity on each graph, dots mark the mean velocity, and triangles mark the $\pm 1\sigma$ confidence limits.

the 59 interevent paths. A posteriori path covariances now form the a priori data covariances $C_{\mathbf{d}}$. The forward problem $\mathbf{G}(\mathbf{x})$ consists of averaging the six regional velocity structures, weighted according to the proportion of path in each region. This was performed as follows: first, the weighted average of crustal thickness was calculated to give the path crustal thickness. The other layer boundaries remained at fixed depths, thus defining the depth extent of all layers. Within each layer, average velocities were calculated for each regional model; the resulting velocity structures were weighted in proportion to path length in each region

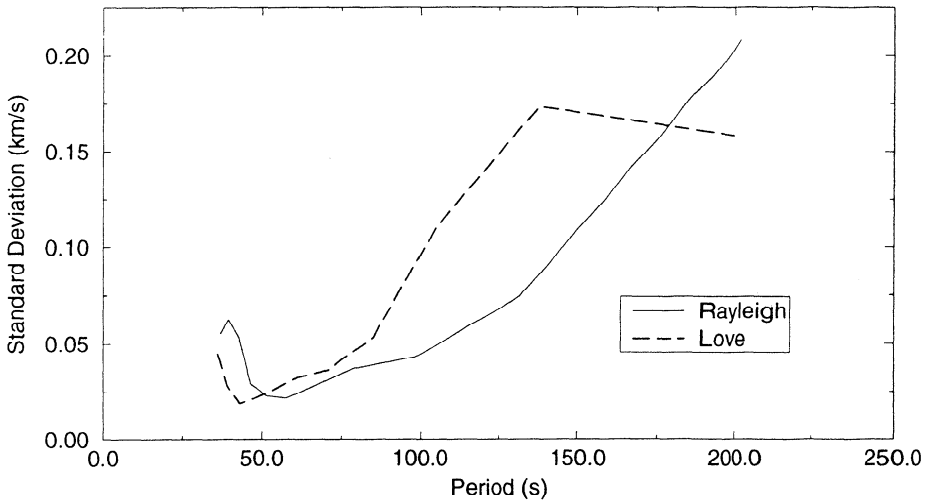

Figure 6. Standard deviation of interevent phase velocities averaged over all paths throughout the Tibetan region used in this study.

and averaged along the path. Hence G is almost linear; the only source of nonlinearity is due to variations in crustal thickness. Hence matrix A in equation (9) is almost constant. However, iterative inversion was again performed to obtain posterior average regional structures.

A Priori Isotropic Shear Wave Velocity Models

Any seismological study using (iterated) linearized inversion theory requires a priori calculation of partial derivatives of seismic velocities with respect to model parameters (equation (9)). If the physical forward theory is nonlinear, partial derivatives calculated for a poor a priori model can direct inversions into secondary minima giving misleading solutions. The Tibetan region contains some of the most anomalous crustal and upper mantle structure on Earth, and hence the quality of prior information $\rho_{\mathbf{p}}(\mathbf{x})$ in equation (5) may have a large influence on our solution.

Curtis [1994] constructed regionalized, isotropic, standardized a priori velocity-depth models for average crustal and upper mantle shear wave velocity structure for the six regions in Figure 7. This was achieved through de-

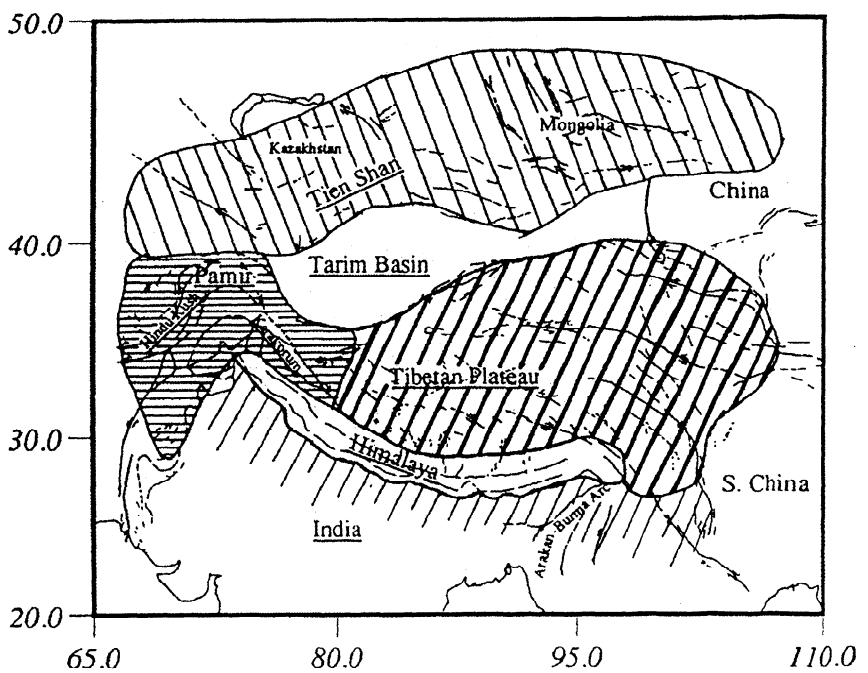

Figure 7. Boundaries of the six regions for which average seismic velocity structure was found. Regions are numbered for future reference as follows: 1, Tien Shan; 2, Tarim basin; 3, Tibetan plateau; 4, Pamir, Karakoram, Hindu Kush region; 5, Himalaya; and 6, Indian shield (including part of southern China).

Table 3. Summary of References Used to Constrain Each a Priori Model

Reference	IN	HY	PL	TB	TS	PM
Avouac et al. [1993]					^{O}	
Barazangi and Ni [1982]		$^{SP}_{M}$	$^{SPAH}_{M}$			
Beloussov et al. [1980]						$^{PH}_{CM}$
Bird [1976]			$^{SH}_{CM}$			
Bird and Toksöz [1977]			$^{SA}_{C}$ $^{S}_{CM}$			
Bourjot and Romanowicz [1992]			$^{SH}_{CM}$			$^{SH}_{CM}$
Brandon and Romanowicz [1986]						
Burov et al. [1990]					^{O}	^{O}
Burtman and Molnar [1993]						^{O}
Chen and Molnar [1975]			$^{SPH}_{CM}$			
Chun and McEvilly [1986]			$^{SH}_{CM}$			
Chun and Yoshi [1977]			$^{SH}_{C}$			
Fan et al. [1994]						^{O}
Grand and Helmberger [1985]				$^{S}_{O}$		
Gupta and Narain [1967]			$^{P}_{C}$			
Hirn et al. [1984]		$^{PH}_{C}$	$^{PH}_{C}$			
Holt and Wallace [1990]	$^{PH}_{M}$	$^{PH}_{M}$	$^{PH}_{M}$	$^{PH}_{M}$		$^{PH}_{M}$
Huestis et al. [1973]	$^{S}_{M}$					
Kosarev et al. [1993]					$^{S}_{CM}$	
Kulagina et al. [1974]						$^{PH}_{C}$
Lepine et al. [1984]		^{H}				
Lyon-Caen [1986]	$^{S}_{M}$	$^{S}_{M}$	$^{S}_{MO}$			
Lyon-Caen and Molnar [1983]		^{O}				
Lyon-Caen and Molnar [1984]				^{O}		
Min and Wu [1987]			^{O}			
Mishra [1981]						$^{H}_{C}$
Molnar [1984]		^{O}				
Molnar [1990]		$^{S}_{O}$	$^{S}_{O}$			$^{S}_{O}$
Molnar and Chen [1984]		$^{S}_{O}$	$^{S}_{O}$			
Ni and Barazangi [1984]	$^{SP}_{M}$	^{O}				
Patton [1980]			$^{SH}_{CM}$			
Pettersen and Doornbos [1987]			$^{S}_{O}$			
Pines et al. [1980]			$^{SH}_{CM}$			
Roecker [1982]						$^{SPH}_{CM}$
Roecker et al. [1993]					$^{SPH}_{CM}$	
Romanowicz [1982]			$^{SH}_{CM}$			
Sapin et al. [1985]			$^{P}_{C}$			
Shaw and Orcutt [1984]			$^{P}_{C}$			
Wang et al. [1992]				$^{S}_{C}$		
Zhao et al. [1992]			$^{SH}_{CM}$			
Zhao and Xie [1993]	$^{PH}_{M}$	$^{PH}_{M}$	$^{PH}_{M}$	$^{PH}_{M}$	$^{PH}_{M}$	$^{PH}_{M}$

Abbreviations are IN, India; HY, Himalaya; PL, Tibetan plateau; TB, Tarim basin; TS, Tien Shan; and PM, Pamir–Hindu Kush. Table elements have the following code: superscripts S, P, H, A refer to S or P velocity, depth to Moho H or attenuation A, respectively, and define the particular aspect of the velocity structure constrained (areas of high attenuation are used only to evaluate uncertainties in structures). Subscripts C,M stand for crust and mantle, respectively, and define the depth range where the S or P velocity or attenuation A is constrained. Subscript O stands for some other, less specific constraint.

tailed review of previous studies on Tibetan structure in the upper 250 km. Seismological inversions for homogeneous models directly estimate the mean velocity structure, whereas heterogeneous models may be spacially averaged to estimate mean structure. Equally important, the set of all models allows us to estimate uncertainties attached to the mean velocity structure. Apart from seismic velocities, constraints can be placed on crustal and upper mantle structure by gravity anomalies, earthquake locations and focal mechanisms, and surface geology. Such information was also used where it usefully constrains some aspect of crustal or upper mantle structure, or gives an impression of structural heterogeneity and uncertainty across a region.

Table 3 summarizes the information used to constrain each model, Table 4 contains the final model parameters and uncertainties, and Figure 8 shows the models themselves. Each model has up to two main crustal and

Table 4. Standardized a Priori and a Posteriori Models

Region	Parameter	Prior Information			Posterior Results		
		Depth Range, km	Value	σ	Depth Range, km	Value	σ
IN	H_c, km		38	15		45.26	3.48
	V_{C1}, km/s	0–H_c	3.71	0.20	0–30	3.54	0.08
	V_{C2}, km/s	unused			30–H_c	3.68	0.19
	V_{M1}, km/s	H_c–155	4.70	0.50	H_c–115	4.34	0.11
	V_{M2}, km/s	155–275	4.62	0.50	115–185	4.69	0.17
HY	H_c, km		55	10		51.64	5.12
	V_{C1}, km/s	0–H_c	3.71	0.20	0–30	3.31	0.10
	V_{C2}, km/s	unused			30–H_c	3.43	0.15
	V_{M1}, km/s	H_c–155	4.70	0.50	H_c–115	4.57	0.21
	V_{M2}, km/s	155–275	4.62	0.50	115–185	4.73	0.24
PL	H_c, km		71	15		73.43	2.32
	V_{Sed}, km/s	0–4	2.50		—		
	V_{C1}, km/s	4–30	3.45	0.15	0–30	3.44	0.04
	V_{C2}, km/s	30–H_c	3.70	0.30	30–H_c	3.44	0.04
	V_{M1}, km/s	H_c–150	4.55	0.20	H_c–115	4.64	0.06
	V_{M2}, km/s	150–250	4.60	0.30	115–185	4.32	0.07
TB	H_c, km		44	10		53.13	6.53
	V_{Sed}, km/s	0–7	2.50		—		
	V_{C1}, km/s	7–20	3.45	0.30	0–20	2.68	0.21
	V_{C2}, km/s	20–H_c	3.75	0.30	20–H_c	2.98	0.25
	V_{M1}, km/s	H_c–120	4.69	0.80	H_c–115	5.40	0.24
	V_{M2}, km/s	120–220	4.46	0.80	115–185	4.48	0.39
PM	H_c, km		70	10		68.80	4.12
	V_{C1}, km/s	0–35	3.48	0.30	0–30	3.43	0.08
	V_{C2}, km/s	35–H_c	3.71	0.30	30–H_c	3.57	0.09
	V_{M1}, km/s	H_c–150	4.81	0.80	H_c–115	4.69	0.12
	V_{M2}, km/s	150–210	4.97	0.80	115–185	4.76	0.11
TS	H_c, km		50	10		42.53	2.96
	V_{Sed}, km/s	0–4	2.58		—		
	V_{C1}, km/s	4–25	3.57	0.30	0–20	3.44	0.14
	V_{C2}, km/s	25–H_c	3.62	0.30	20–H_c	3.60	0.13
	V_{M1}, km/s	H_c–150	4.54	0.80	H_c–115	4.16	0.12
	V_{M2}, km/s	150–300	4.63	0.80	115–185	4.42	0.18

A priori models from *Curtis* [1994]. Region abreviations are as in Table 3, also Sed, sedimentary layer; C1/C2, crustal layers; M1/M2, mantle layers.

two mantle layers (C1, C2, M1, and M2, respectively), with a thin sedimentary layer on top where appropriate. The lowermost mantle layer M2 extends to 220 km, and below this depth all models are fixed at the average continental model PEM-C of *Dziewonski et al.* [1975].

The plateau model PL has a 4 km thick sedimentary layer [e.g., *Chen and Molnar*, 1975] with a positive crustal velocity gradient to a Moho at 71 km. Although various studies detected a zone of low upper mantle velocities, its lateral and depth extent and magnitude are poorly resolved (see references in Table 3). Hence it is not included in the average plateau model, but such a structure lies well within the 1σ uncertainties shown in Table 4.

The Tarim basin model TB contains a deep sedimentary layer (7 km) in accordance with the results of *Wang et al.* [1992]. The only other constraints available are from gravity [*Lyon-Caen and Molnar*, 1984], low resolution surface waves [*Bourjot and Romanowicz*, 1992], low vertically averaged shear velocities from multibounce S waves [*Grand and Helmberger*, 1985], efficient transmission of S_n waves [*Barazangi and Ni*, 1982], and a single crustal thickness estimate in the west [*Zhao and Xie*, 1993]. Hence for the rest of the structure we use the average continental model PEM-C with the estimated crustal thickness and assign large uncertainties to all parameters.

The main seismological constraints in the Tien Shan (TS) show that there are huge variations in structure along the mountain belt [*Roecker et al.*, 1993; *Kosarev et al.*, 1993]. These occur primarily across the Telasso Fergana fault between the western and central Tien Shan, but there may also be significant variation to the east [*Burov et al.*, 1990]. The one-dimensional (1-D) models of *Roecker et al.* [1993] approximately satisfy all other known constraints on the average structure, so we use a four-layer approximation to their shear velocity model with large uncertainties due to the relative lack of information.

The Pamir–Hindu Kush region (PK) has extremely

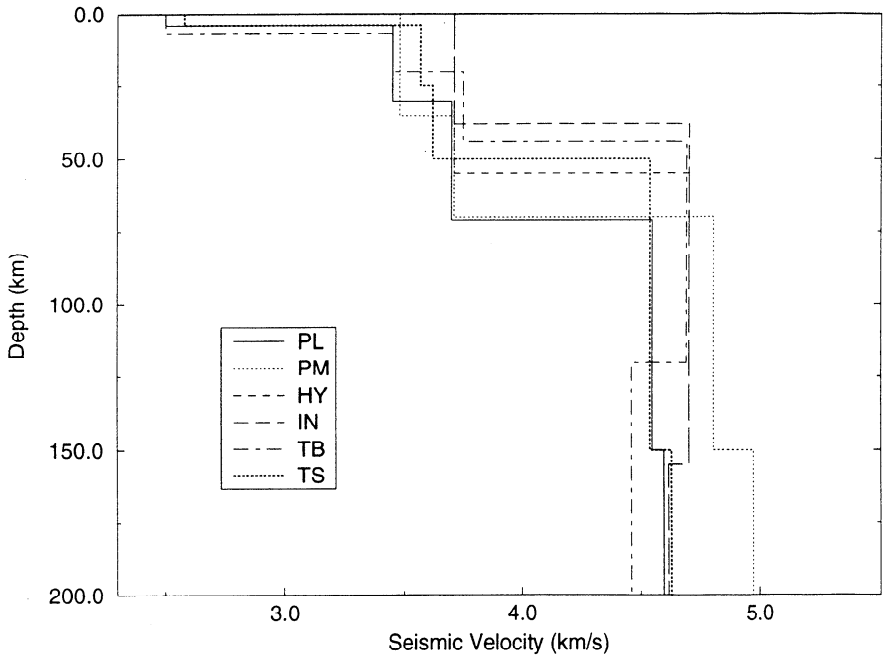

Figure 8. Prior velocity models of the crust beneath the Tibetan region. Abbreviations are: PL, Tibetan plateau; PM, Pamir/Hindu Kush; HY, Himalaya; IN, northern India; TB, Tarim basin; TS, Tien Shan.

complicated tectonic structure with lithosphere subducted from the north and from the south to depths of at least 300 km [*Burtman and Molnar*, 1993; *Fan et al.*, 1994]. Average crustal thickness is around 70 km [*Kulagina et al.*, 1974; *Beloussov et al.*, 1980; *Holt and Wallace*, 1990; *Zhao and Xie*, 1993]. Most seismological studies have constrained P wave velocities. However, *Roecker* [1990] found a 1-D shear velocity profile beneath the Hindu Kush. This model fits all of the other results to within their uncertainties, so we take a four-layer approximation to it with double the uncertainties quoted by Roecker since the model must now accommodate a wider, more diverse area.

The Himalaya (HY) are underthrust by the India shield which dips at between 0° (with a step-like geometry) and 15° beneath the range [*Lepine et al.*, 1984; *Molnar*, 1988]. Other than an increased average crustal thickness of approximately 55 km, constraints on the velocity structure have revealed no significant differences to the northern Indian shield [*Barazangi and Ni*, 1982; *Lepine et al.*, 1984; *Lyon-Caen*, 1986; *Holt and Wallace*, 1990; *Zhao and Xie*, 1993]. The only clear exceptions are the results of *Molnar and Chen* [1984] and *Molnar* [1990], who find higher vertically averaged velocities in the NW Himalaya than elsewhere. Since we require a single horizontally averaged model for the mountain belt we choose the Indian shield model (IN) (see below) with 55 km crustal thickness.

Both *Barazangi and Ni* [1982] and *Lyon-Caen* [1986] measured S_n uppermost mantle velocities beneath the Indian shield of approximately 4.7 km/s. All other results of Lyon-Caen were consistent with a shield model with lid thickness 100–130 km, and we use a four-layer approximation to her best fitting model as our prior information for the northern Indian shield IN.

These models do not provide a complete description of the current state of knowledge of seismic velocity structure across the Tibetan region. However, for the purposes of providing some initial constraints on the magnitude of velocities expected, these models can be used to stabilize and standardize inversions for crustal and upper mantle structure as follows. First, each prior structure was converted into a purely four-layer model with midcrustal and middle/lower mantle depths given in column 6 of Table 4 (this was achieved by averaging the prior model velocities and variances in columns 3–5 over each depth interval in column 6). Then, if γ_j is the proportion of path in region j defined in Figure 7, $\rho_{\mathbf{p}}(\mathbf{x})$ in equation (5) is Gaussian with mean $\mathbf{x}_0$, variance $\mathbf{S}^2$ with

$$\mathbf{x}_0 = \sum_{j=1}^{6} \gamma_j \bar{\mathbf{x}}_j \tag{12}$$

$$\mathbf{S}^2 = \sum_{j=1}^{6} \gamma_j \mathbf{s}_j^2 \tag{13}$$

where $\bar{\mathbf{x}}_j$ and $\mathbf{s}_j$ are the a priori mean and standard deviation of the four–layer approximation for region j.

In what follows it will be shown that the 4–layer prior models account for almost all structure with wavelength > 1000 km wavelengths across the region. Figure 8 also gives an impression of the magnitude of structural variation which might be expected within any velocity inversion. Crustal thickness varies by at least 35 km across

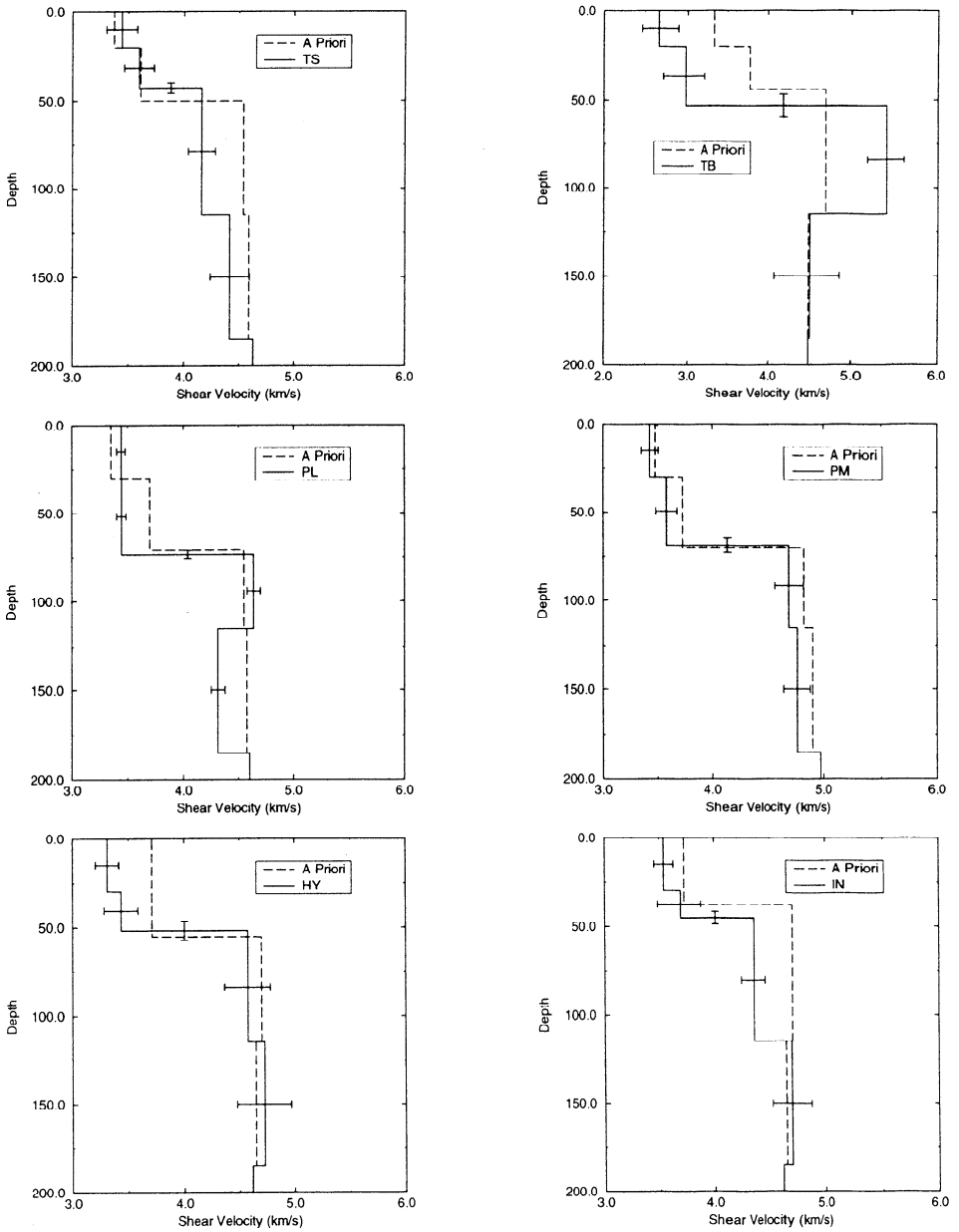

Figure 9. Posterior average shear velocity models in regions TS, Tien Shan; TB, Tarim basin; PL, Tibetan plateau; PM, Pamir/Hindu Kush; HY, Himalaya; and IN, India. Error bars are as in Figure 10.

the Tibetan region, crustal velocities by over 1 km/s, and upper mantle velocities by around 0.5 km/s. Also, since the models themselves are averages, these values should be regarded as minimum estimates of possible variation.

Results

First, we examine long traverses (approximately > 1000 km) across the Tibetan region which give broad averages of structure over different geological provinces. We then refine this overview with structures along shorter paths and from the regionalization in the Tien Shan, Pamir-Hindu Kush, Tarim basin, Himalaya, southeastern region, the Tibetan plateau, and the Indian shield (where the southeast region refers to the relatively dense area of paths in the southeast of Figure 4).

Each structure shown from Figure 9 onward has four layers: the upper crust (C1) extends from the surface to a depth of 20 km (for models TS–Tien Shan and TB–Tarim basin) or 30 km (all other regional and all path models), the lower crust (C2) has lower boundary at the Moho with depth H_c, the uppermost mantle layer (M1) extends to a depth of 115 km and the lower layer (M2) reaches a depth of 185 km. Between 185 km and 220 km, all models are held fixed at their a priori values, and beneath this level all models have the velocity structure of PEM–C [*Dziewonski et al.*, 1975]. Only shear velocities were varied independently. P velocities were constrained by the ratios

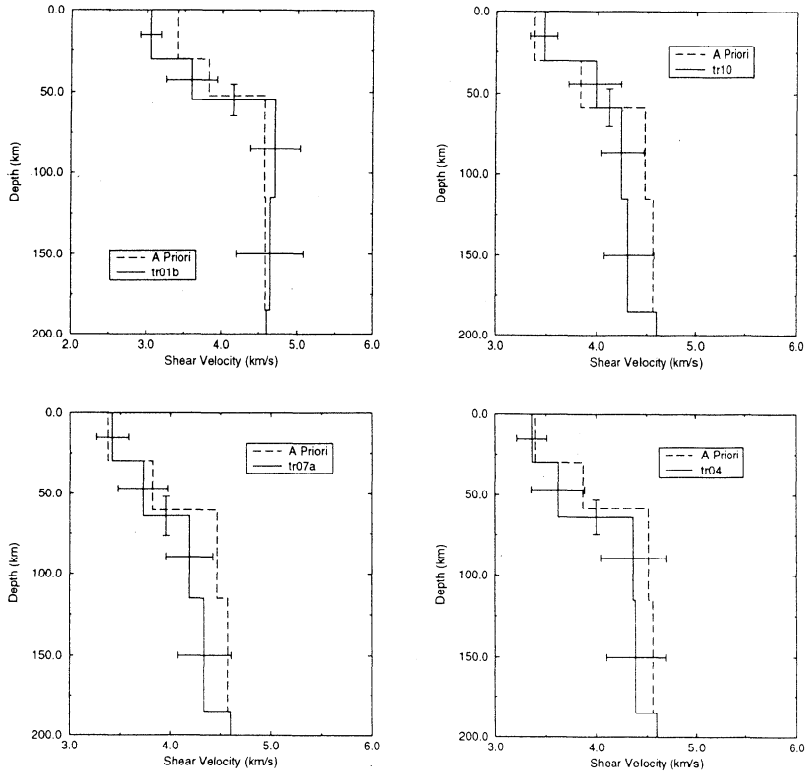

Figure 10. Average shear velocity models along paths tr01b, tr07a, tr10, and tr04 as referenced in Figure 4 and Table 1. Error bars are formal 1σ bounds.

$$\frac{V_P}{V_S} = \begin{cases} 1.73 & \text{in the crust} \\ 1.8 & \text{in the mantle} \end{cases} \quad (14)$$

as used by *Chen and Molnar* [1981]. Phase velocities are relatively insensitive to density structure so this was fixed by averaging PEM–C in each layer, as was the quality factor Q. Repeatability between paths traversed by more than one event pair was generally excellent with crustal velocity variation of only 0.1 km/s, mantle velocity variation of 0.2 km/s and variation in H_c of only 5 km (shown explicitly below for plateau paths). Hence we present models which represent median structures on each path.

Average path velocity structures were regionalized using the theory described earlier. The structures along paths hy03 and se11 are anomalous (see below) and proved to bias considerably the average Indian and Himalayan structures. Hence they were omitted from the regionalization and results are shown in Figure 9 and listed in Table 4.

Another regionalization was carried out with variances attached to all prior information increased by a factor of 4. Model estimates in all regions other than the Tarim basin did not vary noticeably and uncertainties were only slightly increased. The Tarim basin model remained within the 1σ uncertainties shown below. Hence models shown are not significantly restricted by prior information. Finally, iterative regional inversions were performed to test the degree of non-linearity introduced by crustal thickness parameters. The results, tabulated by *Curtis* [1994] and reported below, showed Gaussian variation of all parameters almost entirely within $3\sigma/2$ limits of models shown here, verifying the approximate linearity of regionalization.

Long Traverses ($\sim$ 2000 km). There are 13 distinct long traverses with references beginning "tr" in Figure 4. Almost all models lay within one standard deviation (1σ) of their respective a priori models, and Figure 10 shows those that did not. Path tr01b mainly traverses the eastern Tien Shan and the Tarim basin, and its upper crustal velocity is significantly lower. Traverse tr04 crosses the Tarim basin and Tibetan plateau and seems to require a lower C2 velocity than the a priori model. The velocity in layer M1 of path tr07a deviates from the a priori model by more than one standard deviation. Also, the easternmost traverse, tr10, exhibits a mantle velocity structure which is consistently lower than the a priori model by one standard deviation. However, apart from the low velocity crust along path tr01a, none of these features are unequivocally resolved. Hence at length scales greater than approximately 1000 km, the a priori information gathered in Table 3 is almost sufficient to represent regional velocity structure with depth.

Tien Shan. There are three interevent paths which lie entirely within the Tien Shan region, with structures shown in Figure 11. These paths are quite similar in structure, and certainly all overlap at the 2σ level. Crustal thickness seems to be greater along ts03a than along the other paths ($\sim$60 km rather than $\sim$50 km)

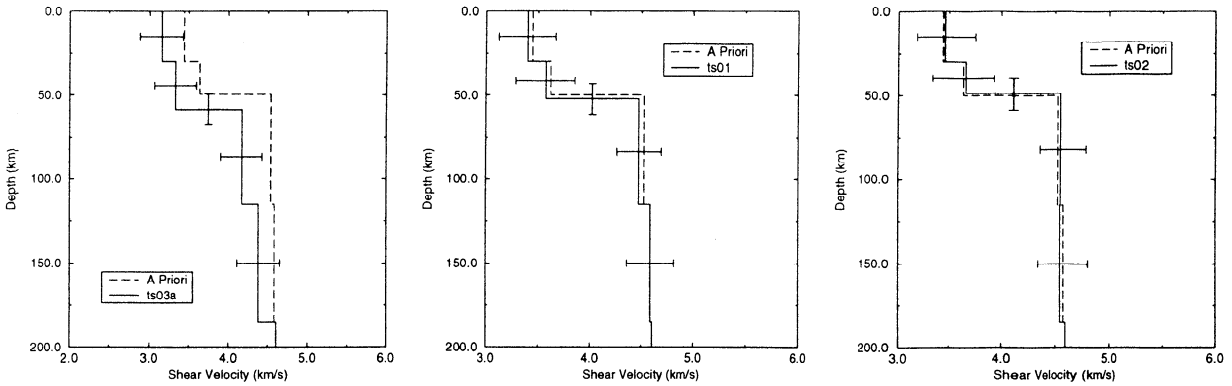

Figure 11. Average shear velocity models along paths ts03a, ts01, and ts02 (from west to east along the Tien Shan mountain range), with error bars as in Figure 10. Notice the extended range on the velocity axis in the right hand figure.

with a suggestion of lower crustal and uppermost mantle velocities. However, this path is very short so that phase additivity may not be so readily assumed between the two event-station paths and event mislocation may cause significant errors. Hence we treat this structure with more scepticism than the others.

The Tien Shan regional average model deviates from the a priori model by up to $\frac{5}{2}\sigma$ (Figure 9). The results show a well-resolved thinner crust (43 km), probably due to the eastern section of the region where topography is less extreme and hence may not have undergone such extensive lithospheric shortening and thickening.

There is also a well-resolved low uppermost mantle velocity. A low M1 velocity was observed along path ts03 in the western Tien Shan, but its persistence in the regional model suggests that it must be compatible with the numerous long traverses over the eastern Tien Shan. Low M1 velocities are not, however, observed along paths ts02 or ts03 in the north central and northeastern Tien Shan. Hence there appear to be two zones of low M1 velocity, one in the area around ts03 and the other in the east, separated by higher velocities, but it is possible that the two low-velocity zones join along the southern Tien Shan.

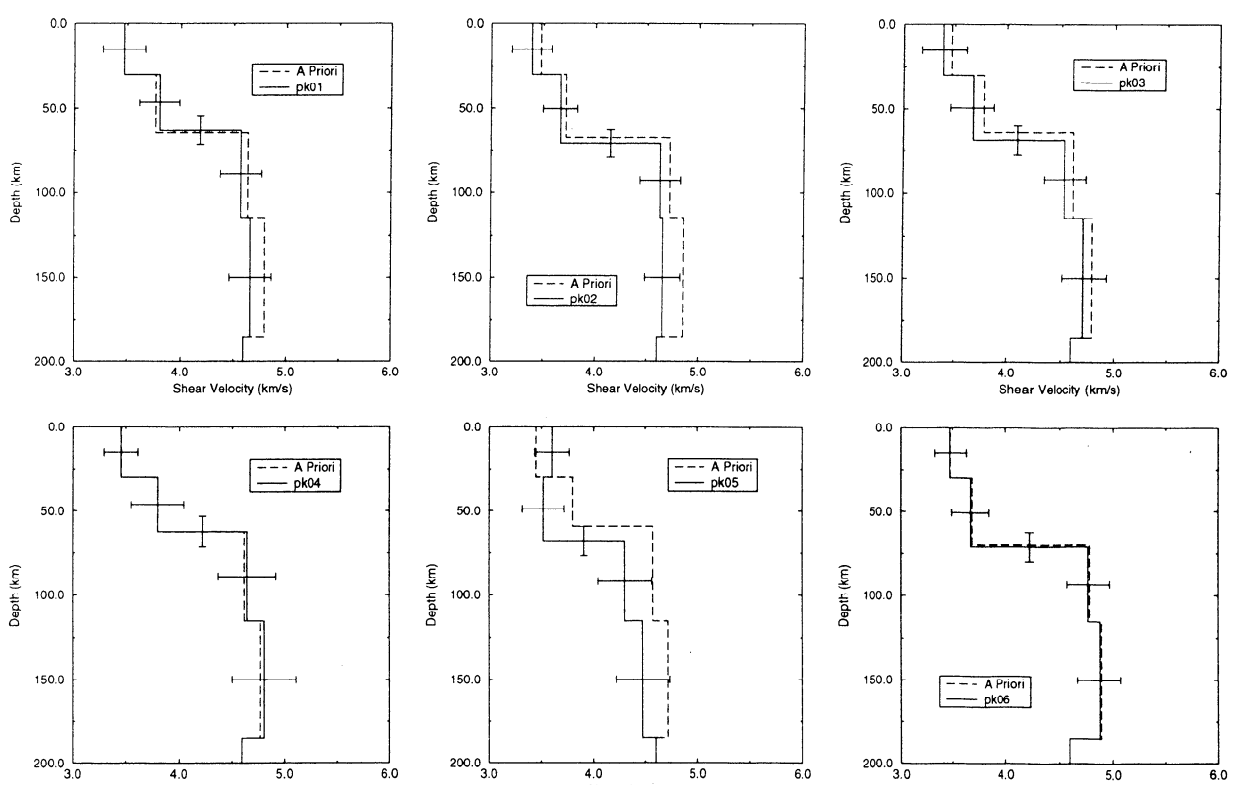

Figure 12. Average shear velocity models along paths pk01, pk02, pk03, pk04, pk05, and pk06, with error bars as in Figure 10.

Pamir and Hindu Kush Region. Six paths traverse this region of which four are almost pure (pk01, pk02, pk03, and pk06), the other two crossing a significant portion of the south-western Tien Shan (pk04 and pk05). The structures along these paths are shown in Figure 12 and are all similar to within approximately 1σ. Five of the six paths show very similar structures to the a priori models. Path pk05 in the eastern Pamir/western Tien shan, however, exhibits greater crustal thickness (~70 km rather than 60 km) and mantle velocities reduced by around 0.3 km/s, resembling the structure on the neighbouring Tien Shan path ts03a.

The average regional Pamir–Hindu Kush model PM is almost unresolveably different from the a priori model (Figure 9). However, lower velocities throughout all layers would better suit the data, most noticeably in the lower crust. Low velocities remain when the a priori information is weakened, and uncertainties do not noticeably increase. As described earlier, the tectonic structure in this region is complex so that surface wave data presented here cannot provide any extra tectonic information. However, the model PM provides an average structure which may be useful in future large-scale seismological studies.

Tarim Basin. The Tarim basin contains no pure paths: its structure is constrained by the regionalization alone. The average Tarim basin model TB exhibits a very different structure, parts of which seem to be well-resolved despite large uncertainties. Figure 9 shows very low average velocities in the Tarim crust. Fluctuations in the iterative regionalization showed that V_{C1} varied between 2.6 km/s and 3.0 km/s, whereas V_{C2} varied between 2.8 km/s and 3.6 km/s. Hence lower crustal velocity is significantly lower than the prior shield structure (in which V_{C2} was estimated at 3.8 km/s) but may be slightly higher than that shown. The crustal thickness of 53 km is poorly constrained with fluctuations of around ±15 km observed in the iterative procedure.

Upper mantle velocities show a lid type structure with an extremely high-velocity lid (~5.2 km/s), which increases when the a priori information is relaxed, wherea normal shield velocities are observed in the lower mantle layer (~4.5 km/s). Although iterative fluctuation in V_{M1} is up to 1.2 km/s in magnitude, the minimum value of this velocity is 4.9 km/s which is still significantly higher than the prior information suggested. Fluctuations in V_{M2} are all less than 0.6 km/s, and the velocity has a maximum value of 4.6 km/s.

Hence the slow crustal and fast uppermost mantle velocities and the negative mantle velocity gradient with depth are all formally well-resolved. However, the fact that all constraints are imposed along long paths which traverse at least two other regions makes this result susceptible to errors from more sources than for the other regional structures. The a priori estimate of crustal thickness can not be revised using the current data.

Himalaya. Paths hy01 and hy05 traverse the Himalaya mountains along strike for about 1000 km and

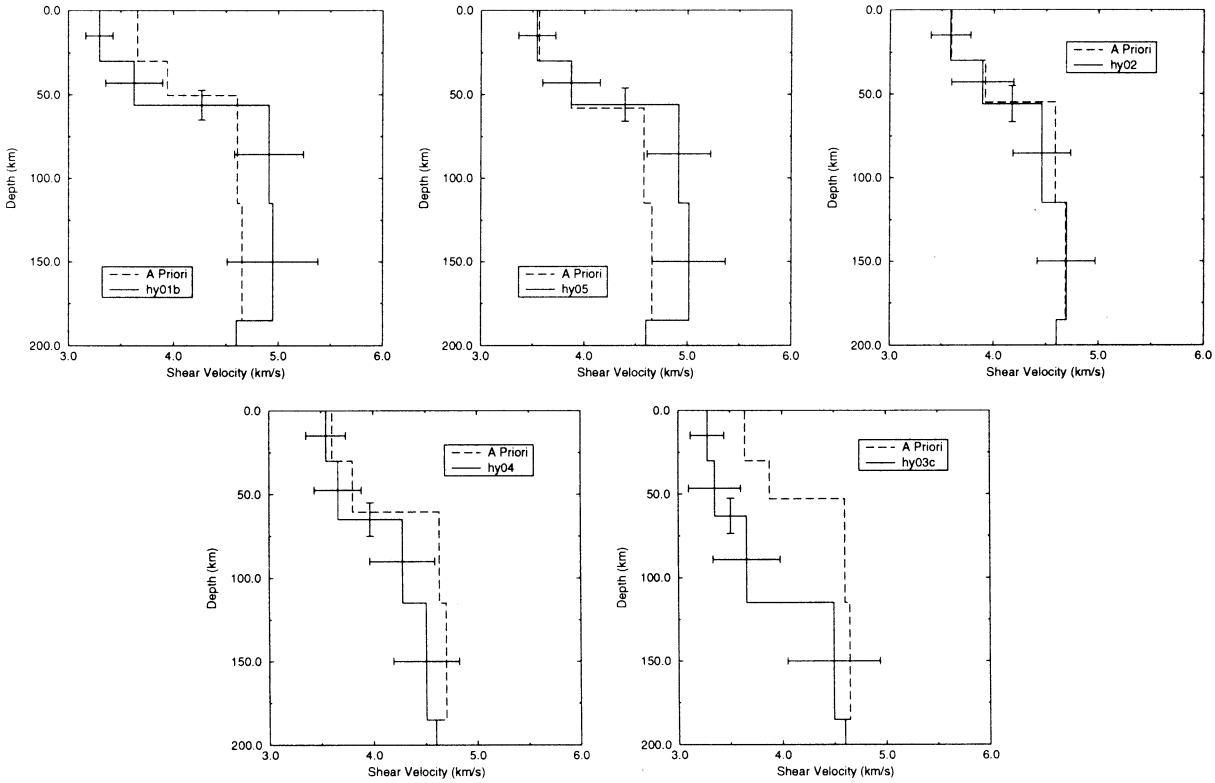

Figure 13. Average shear velocity models along paths hy01b, hy02, hy03c, hy04, and hy05, with error bars as in Figure 10.

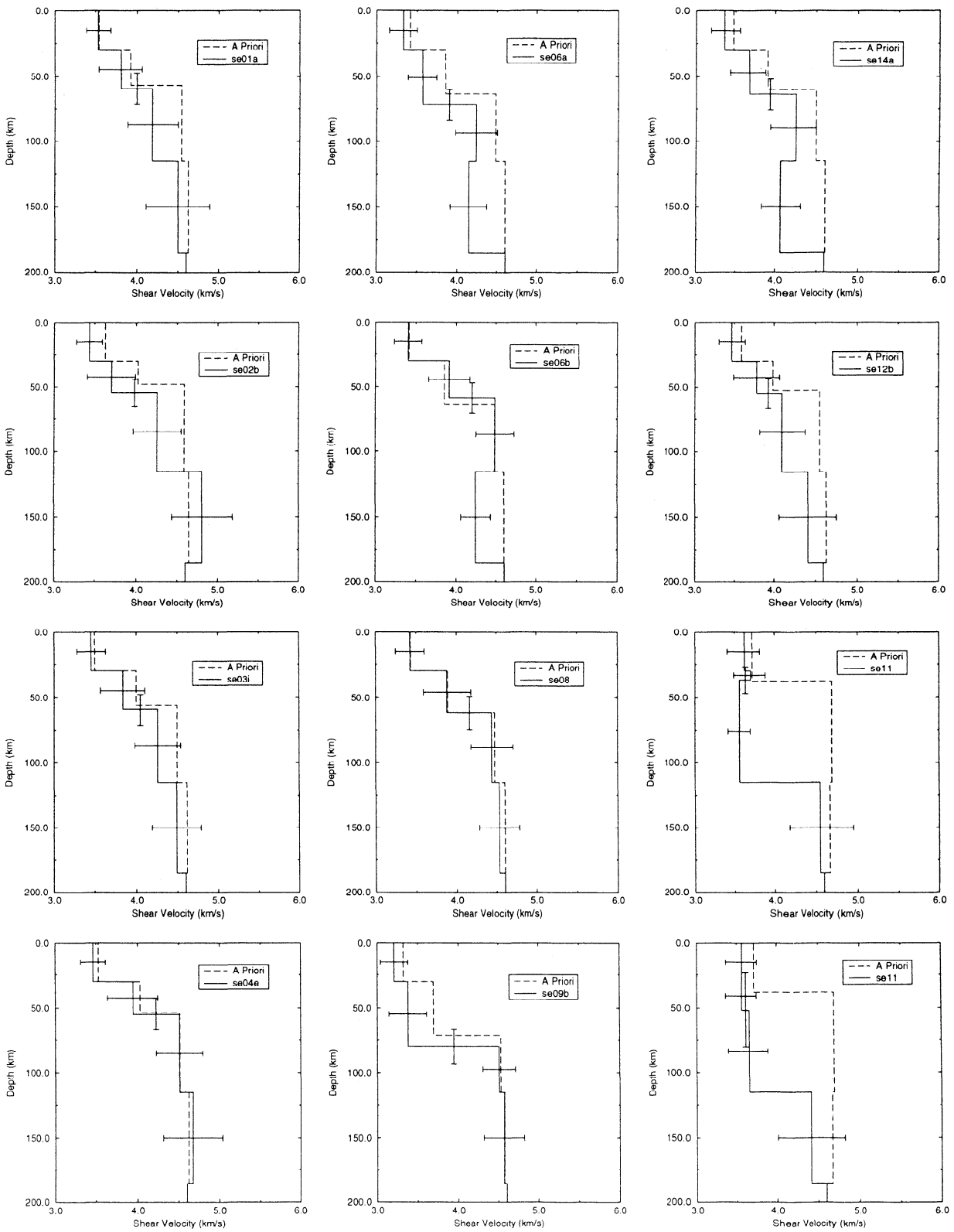

Figure 14. Average shear velocity models along paths se01a, se02b, se03i, and se04e; se06a, se06b, se08, and se09b; se11, se12b, and se14a, plus in the lower right-hand corner, average shear velocity model along path se11 when the a priori standard deviation attached to crustal thickness is increased from 10 km to 30 km; listed in three columns, respectively, with error bars as in Figure 10.

extend farther to the SE and NW, respectively. Crustal velocities are lower, and crustal thickness is greater along path hy01 (Figure 13), suggesting a deeper crust in the Arakan-Burma range, southeast of the eastern Himalayan Arc. Upper mantle structures are similar, and both are higher than the a priori model by about 0.4 km/s (1σ). Path hy04 traverses the same section of the Himalaya and has similar crustal structure but lower mantle velocities than the a priori. Hence if the high velocities along hy01 and hy05 are real, either they must come from the path sections outside of the Himalaya range or the mantle structure of path hy04 must be in error by around 2σ.

Around a third of path hy02 traverses the Indian shield, and its structure lies very close to the a priori model. However, path hy03 transects the Himalaya with about one third of its length in India and exhibits extremely low crustal and M1 velocities. This path will be discussed further below.

The main deviation of the regional average model HY from the prior information in the Himalayas is the existence of low velocities in the crust (Figure 9). These average at approximately 3.3 km/s, and they are maintained to within $\sigma/2$ when the a priori information is relaxed. Posteriori covariances show a relatively strong correlation between H_c and V_{M1} of model HY and between V_{M1} of model HY and H_c of the Indian model IN. The iterative procedure showed that V_{C1} and V_{C2} rarely assume values larger than 3.35 km/s and 3.5 km/s, respectively. Hence the low crustal velocities are well-resolved, but the prior crustal thickness estimate cannot be revised with the current data.

Southeast Region. Paths in this area were generally repeated by several different event pairs, and structures are shown in Figure 14. Only one path showed inconsistant structures between traverses (se06a,b), and we could find no reason to favor one or the other, so both are shown in Figure 14. Paths se02, se03, and se04 are repeated 3, 7, and 4 times, respectively; each have excellent repeatability and hence are more tightly constrained than their uncertainties suggest. Paths se02, se03, and se04 fan out to the south and southwest from a single point NE of the Arakan–Burma Arc and most of path se08 traverses the same region. Differences between all parameters are unresolvable at the 1σ level and show an average crustal thickness of approximately 60 km.

Of the paths which traverse part of the plateau region, paths se06 and se14 penetrate the Chang Thang area, farther to the north than paths se01 and se12. The main feature common to se06 and se14 is a velocity inversion between layers M1 and M2 forming an upper mantle lid structure. Structures se01 and se12 agree to within $\sigma/2$ and exhibit no such velocity inversion. Thus the lid structure is confined to the north central plateau.

Paths hy03 and se11 show similar structures with much lower M1 velocities than any other paths in this study. This is not a consequence of over-restrictive constraints on the prior crustal thickness since increasing the prior standard deviation of H_c by 300% did not significantly change the model (Figure 14). It is not impossible that such a low-velocity upper mantle does exist in and south of the eastern Himalaya since paths se01 and se12 also exhibit structures with low M1 velocities. Alternatively, there may be some uncommonly large perturbation in either the V_p–V_s ratio or the density structure in these regions which are not allowed to vary independently in the current inversions.

The average Indian model IN (for which paths hy03 and se11 were calculated) is predominantly effected by the southeast area. Crustal thickness has increased to 45 km in model IN. Lower crustal and the lowermost mantle velocities remain almost unchanged. Upper crustal and uppermost mantle velocities are significantly lower than the prior model with values of approximately 3.5 km/s and 4.3 km/s, respectively, $\frac{3}{2}\sigma$ and $\frac{5}{2}\sigma$, respectively, away from the a priori model values.

The crustal thickness of model IN is thinner than all of the paths in the south-east area since the Indian region includes paths which traverse areas of thinner crust in the stable Indian shield. It is likely that the low M1 velocities exhibited by model IN are compensating for the diminished crustal thickness. As noted above, trade-off between crustal thickness of this model and V_{M1} of the Himalayan model HY is large (and negative), as is the (positive) trade-off between H_c and V_{C2} in model IN. Hence an increase in crustal thickness in the Indian region would lead to a decrease in Himalayan uppermost mantle velocity and an increase in Indian uppermost mantle velocity, making the average Himalayan and Indian mantle velocity structures unresolveably different.

Tibetan Plateau. In Figure 15, structures for all event pairs are shown for paths across the Tibetan plateau, rather than only median structures. This gives a concrete example of result repeatability with different event pairs over the same geographical traverse.

There are four geographically distinct paths, pl01 to pl04, and paths pl03 and pl04 are repeated. Neither of the repeated paths shows significant fluctuation in any parameter. Crustal velocity measurements differ by up to 0.1 km/s, mantle velocities by up to 0.2 km/s, and crustal thickness by less than 2 km for path pl03 and less than 5 km for path pl04. This level of variability is similar to that observed along almost all repeated traverses and is taken to represent parameter uncertainties due to event mislocations, source time error, or noise which survived the time variable filtration.

Paths pl02, pl03, and pl04 show crustal thickness of around 78 km, whereas path pl01 has a thinner crust (70 km). Hence there is a suggestion of decreased crustal thickness in the NW, but constant crustal thickness elsewhere beneath the plateau. Crustal and M1 velocity structure is similar across all four paths, but M2

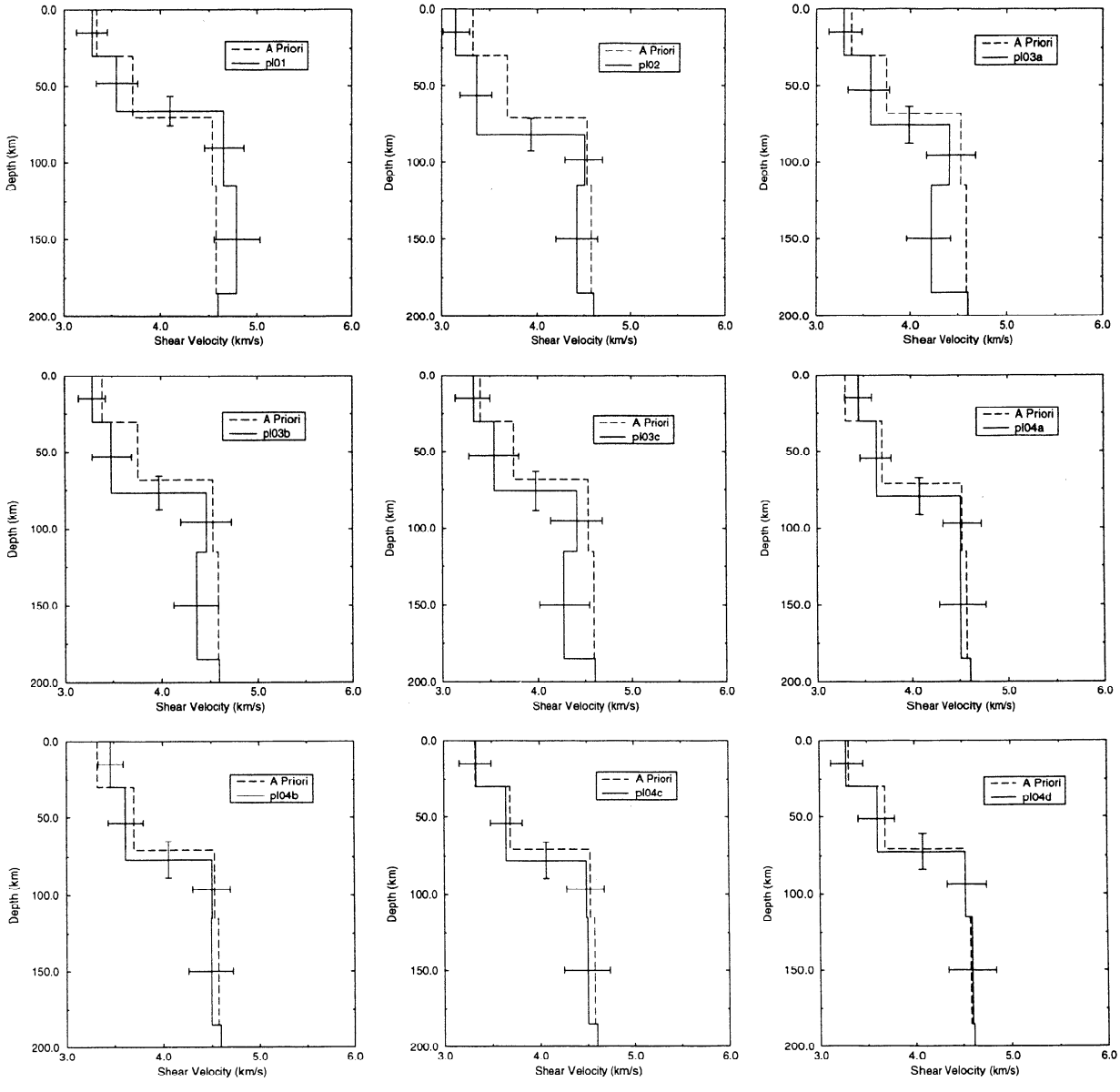

Figure 15. Average shear velocity models along paths pl01, pl02, pl03a,b,c, and pl04a,b,c,d with error bars as in Figure 10.

velocities have a wider range (4.15 4.6 km/s). Paths pl01 and pl04 in the northwest and east exhibit a positive or zero mantle velocity gradient, whereas paths pl02 and pl03 show a mantle velocity inversion forming an upper mantle lid.

All parameters of the plateau regional average model PL are extremely tightly constrained (Figure 9). Crustal velocity is almost constant at 3.4 km/s to a depth of 73 km. A lid type structure is well resolved in the upper mantle, and the lowermost mantle velocities of 4.3 km/s are the lowest found in this study. Iterative fluctuations of all parameters were within 1σ.

The constant crustal velocity of model PL was not observed along any pure plateau (pl) paths, nor along any paths which entered the plateau region (tr or se). In order to investigate the cause of this structure, two more PL structures were calculated by regionalizing first with long traverses excluded and second with southeastern paths excluded. A third structure was calculated which is the average from only pure plateau paths, and all three are shown in Figure 16.

A comparison of these three plots with the PL structure in Figure 9 shows that the long traverses are mainly responsible for the uniform crustal velocity, although southeast paths also contribute. Also, posteriori covariances show that the PL structure does not trade off significantly with other regional structures. Hence since the majority of mixed paths traverse the east central plateau region which is not traversed by a significant length of any pure plateau paths, there appears to be strong evidence for a zero crustal velocity gradient in this area.

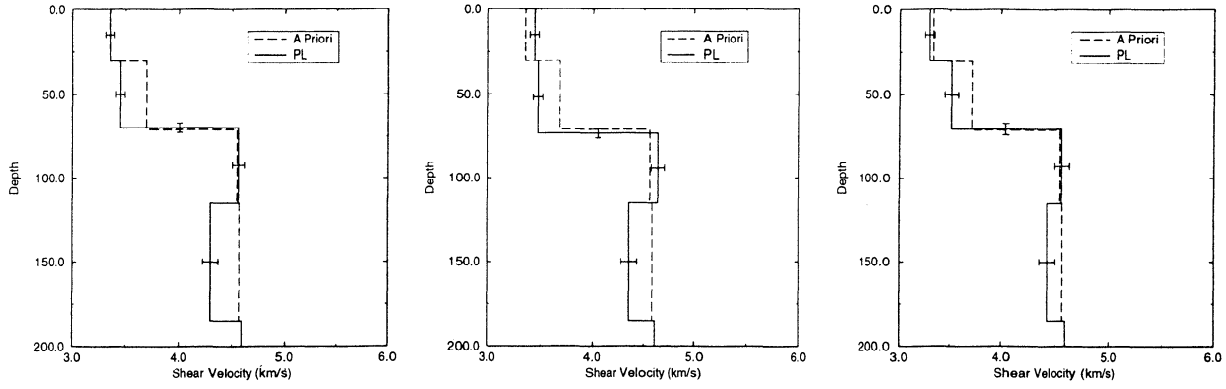

Figure 16. Average shear velocity models in the plateau region: (left) structure when all long traverse (tr) paths are omitted from the regionalization, (middle) when all southeast (se) paths are left out, and (right) the average structure from the plateau (pl) paths alone. Error bars are as in Figure 10.

The upper mantle lid structure was observed along the two central plateau paths pl02 and pl03, and along paths se06 and se14, but not along paths pl01 and pl04. The lid structure is tightly constrained in model PL and must have been required by many of the long traverses. Hence the geographical extent of the lid structure may be estimated. It certainly seems to lie beneath the central and northeast central plateau (from structures pl02, pl03, se06, and se14), and because the majority of the mixed paths traverse the eastern plateau, it is probable that the lid extends at least as far to the east as the northern half of path pl04. The average structure along path pl04 (which was traversed by four different event pairs) indicates that the zone does not extend along its entire length, and the structure observed along pl01 (an unrepeated path) suggests that it may not extend to the west or northwest plateau. Finally, the low-velocity zone is not observed along paths tr11, se01, and se12 and hence probably does not extend to the southern or southwestern plateau.

Interpretation and Discussion

Our analysis contains some key assumptions. First, we assume that 30 s to 200 s period surface waves travel along great circle paths. This is reasonable for short paths but may cause some bias in our results for long paths. Second, we do not explicitly assess uncertainties in earthquake source locations. The effect of source phase errors will be inversely proportional to distance and hence should only significantly effect shorter paths. In addition, repeatability between different event pairs was excellent as illustrated above explicitly for Tibetan plateau paths, illustrating that this effect may not be large. Finally, we neglect the effect of anisotropy, primarily because of the low number of interevent paths. *McNamara et al.* [1994] showed that anisotropy may be significant beneath the plateau but that the fast direction of propagation varies laterally by up to 90°. Hence our isotropic results should not be overly biased since the paths used have a prevelent SSE trend and span regions where this trend is aligned with both fast and slow directions. Our most robust results are summarized below.

In the Tien Shan, both *Roecker et al.* [1993] and *Kossarev et al.* [1993] found low and high P wave velocities throughout most of the crust and upper mantle to the east and west of the Telasso–Fergana fault respectively, with contrasts in the mantle of up to 0.7 km/s to at least 150 km depth. In the current study, the westernmost (pure) Tien Shan path, ts03, exhibited crustal and upper mantle S velocities on average 0.4 km/s lower than those on either the central or eastern paths ts01 or ts02, respectively. Under the ratio $V_P/V_S = 1.8$ used earlier, this corresponds to a P wave velocity difference of 0.72 km/s which matches the contrast that Roecker et al. observed to the west of ts03.

The similarity in structure between paths ts03 and pk05 but not pk04 or ts01 suggests that the low-velocity zone extends southeast of the Telasso–Fergana fault toward but not far into the Pamir region and does not extend far to the northeast. Also, the regional structure TS in conjunction with pure Tien Shan path structures provides evidence for a second zone of low upper mantle velocity in the eastern Tien Shan region with a probable decrease in crustal thickness. The high uppermost mantle velocity in the Tarim basin structure TB shows that the low velocity zones can not extend southward over a large area, except perhaps in the far western Tarim where there are no paths.

Roecker et al. [1993] interpreted the area of low velocities as a region where the lithospheric upper mantle had been advected downward and westward, being replaced by upwelling hotter and seismologically slower aesthenospheric material, also corroborated by S splitting results [*Makeyeva et al.*, 1992]. The results here suggest that the area over which upper mantle material has been removed may not extend for more than approximately 1000 km along strike of the mountain belt (Figure 17). If mantle material is upwelling be-

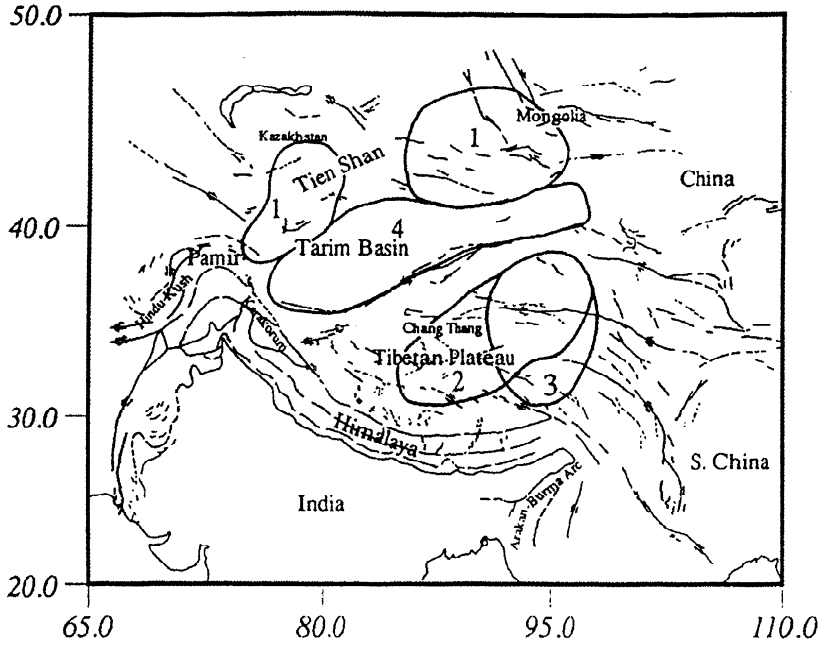

Figure 17. Best estimates of the geographical extent of high- and low-velocity zones within the Tibetan region, based on results from this study. Key to shaded areas: 1, low average upper mantle velocities beneath the Tien Shan; 2, lowest mantle velocities beneath the plateau beween 115 and185 km; 3, zero crustal velocity gradient with depth; 4, high uppermost mantle velocities.

neath the central Tien Shan, we might also expect a potential gradient to exist eastward causing an eastward flow of mantle material. If the higher velocities along paths ts01 and ts02 are caused by mantle material displaced eastward, then this material does not extend to the far eastern Tien Shan (Figure 17). Since the displaced material must go somewhere, we suggest that it sinks downward since it is relatively cool and negatively buoyant. This in turn could explain the eastern low-velocity zones: entrained eastern lithospheric mantle would move westward and sink, causing a second low-velocity zone of mantle upwelling in the east. This would complete an along-strike convection cell system [*McKenzie et al.*, 1974; *Molnar*, 1992].

The Tarim basin is an area for which very little seismological information was available. *Burov et al.* [1990] found that a flexed plate model with elastic thickness of 50–60 km provided the best fit to gravity data in the northern Tarim, and at a single point in the western Tarim, *Zhao and Xie* [1993] found the crustal thickness to be 44±7 km. These estimates could not be revised in the current study, and due to the many sources of error for the Tarim structure discussed earlier, the results obtained here should be regarded as preliminary. However, a distinctive velocity structure is observed in the average model for the region TB, that is, average upper crustal velocities are extremely low (< 3.0 km/s) within the top 30 km, probably a reflection of up to 15 km of sediment [*Wang et al.* 1992]. However, lower crustal velocities are also significantly lower than the average shield structure.

In contrast, uppermost mantle velocity is extremely high, and exhibits a pronounced lid structure (Figure 17). *Barazangi and Ni* [1982] observed that S_n waves propagate across the basin with little attenuation. Together these observations might suggest that the lithospheric mantle beneath the cratonic Tarim basin is cooler than the surrounding regions: assuming the upper mantle composition of *Duffy and Anderson* [1989], the shear velocity/temperature gradient is approximately 0.1 km/s per 300°C. This would imply an uppermost mantle temperature decrease of 300–600°C beneath the Tarim basin compared with either the Tien Shan or the Tibetan plateau.

However, because of inherent trade-offs in the resolution of phase velocity data, to first order we may decrease this velocity if we increase the layer thickness without significant deterioration in data fit. A simple calculation shows that to reduce the velocity to that of the continental model PEM-C [*Dziewonski et al.*, 1975], the layer would have to be ~ 180 km thick. First-order theory breaks down with such a large perturbation, but we can not rule out some substantial increase. Thus, if the base of the lid structure signals the base of the lithosphere, either the uppermost mantle lithosphere beneath the Tarim basin is extremely fast compared to average continental or oceanic models or the lithosphere is very thick.

The Tibetan plateau models in Figures 9 and 16 provide strong evidence for a zero velocity gradient with depth throughout the 73 km thick crust in the east central plateau but a positive velocity gradient throughout

a thinner crust farther west and southeast (Figure 17). *Chun and Yoshii* [1977], *Romanowicz* [1982], and *Brandon and Romanowicz* [1986] found average crustal velocity to be 3.4–3.5 km/s, consistent with the crustal velocity of model PL which averages at 3.44 km/s. The average plateau mantle structure exhibits a definite lid structure (Figure 17), inferred by both *Zhao et al.* [1991] and *Lyon-Caen* [1986]. The lid velocity of 4.64 km/s in model PL lies within their estimates of 4.6–4.7 km/s.

Brandon and Romanowicz [1986] observed the upper mantle lid structure beneath the Chang Thang area of the plateau. The results found here suggest that the zone covers most of the central and north–central plateau, in agreement with the area of high $S-P$ residuals found by *Molnar and Chen [1984]* and high S residuals observed by *Molnar* [1990] and may also extend to the northeast plateau to approximately 96°E (Figure 17). *Molnar* [1990] suggested that the zone does not extend to the Himalayan thrust front, but the current results also suggest that it does not extend to the southern plateau beneath paths tr11 in the south or paths se01 and se12 in the southeast plateau (Figure 4).

Barazangi and Ni [1982] observed inefficient transmission of S_n waves over the Chang Thang area, whereas *McNamarra et al.* [1994, 1997] observed a more extensive zone covering much of the north and central plateau. The area of zero crustal velocity with depth roughly coincides with both the area of inefficient S_n transmission and with surface observations of subrecent basaltic volcanism [*Burke et al.*, 1974; *Kidd*, 1975; *Şengör and Kidd*, 1979; *Molnar et al.*, 1987]. We propose that basalt may be injected from the uppermost mantle into the plateau lower crust as molten intrusions, and some is ejected volcanically at the surface. The basalt intrusions provide an additional heat source in the lower crust, steepening the geothermal gradient. This in turn reduces the velocity gradient with depth explaining the constant average velocities throughout the crust. The extra basaltic fluid in the upper mantle and possible associated partial melting at the Moho [*Bird and Toksöz*, 1977] would explain the inefficient transmission of S_n waves through the region.

The average crustal and uppermost mantle velocity structure of the Pamir–Hindu Kush region (hereafter referred to as the Pamir region) is unresolveably different from the plateau structure. Crustal thickness estimates of ~70 km beneath the plateau and Pamir decrease to 60 km beneath the western Tien Shan and ~42 km beneath central Tien Shan. Average velocities between 115 and 185 km are significantly higher beneath the Pamir than beneath the Tien Shan or Tibetan plateau. This probably reflects subduction of the Asian and Indian plates which transports cold, fast lithospheric material to depths of 300 km or more beneath the Pamir [*Burtman and Molnar*, 1993; *Fan et al.*, 1994].

Underthrusting of the Entire Tibetan Plateau? Differences between average crustal structures in models IN, HY, and PL are probably unresolveable, apart from a definite increase in crustal thickness beneath the plateau. The M2 layer velocities of models IN and HY are unresolveably different due to large trade-offs between M1 velocities of model HY and crustal thickness of model IN. Hence apart from crustal thickness variations, the crustal and uppermost mantle structure beneath the Tibetan plateau, Himalaya, and southeast region are not resolveably different. However, the north and central plateau model exhibits a pronounced lid structure which does not exist further south.

Barazangi and Ni [1982] observed S_n velocities of 4.74 km/s across the plateau and 4.69 km/s beneath the Indian subcontinent and inferred that the Indian shield (crust and mantle) must have underplated the plateau. S_n waves sample the uppermost mantle, and the value of 4.74 km/s is similar to the tightly constrained M1 velocity of the average plateau model PL. Hence the current results are consistent with those of Barazangi and Ni.

The Indian shield is known to underthrust the Himalayan range from the numerous, consistent subduction-related fault plane solutions of earthquakes. Therefore models HY and IN represent the upper mantle velocity beneath the Indian subcontinent. The M1 velocity of HY is unreliable due to trade-off with model IN, but if the M1 velocity of 4.69 km/s observed by *Barazangi and Ni* [1982] is correct, then the M2 velocity in models HY and IN (4.7 km/s) suggest a negligible velocity gradient with depth beneath the Indian shield.

This upper mantle structure is not observed beneath the Tibetan plateau. Hence either the Indian shield (including layer M2 since there is no definable lid structure to mark the base of the lithosphere) has underthrust the plateau and the faster M2 layer observed farther south has been removed or alterred in such a way that it has become much slower, or the Indian shield has not penetrated far beneath the plateau and the low velocities observed in model PL represent the current state of the upper mantle beneath the Asian crust. A structure consisting of the entire Indian shield underplating the Tibetan crust is not consistent with the current results, unless the coherently moving Indian lithosphere is less than approximately 85 km thick.

Conclusions

The following are the main results and conclusions which have been drawn from work in the current study:

1. A detailed review of previous seismological studies was used to construct six "standardized a priori" models for the Tien Shan, Tarim basin, Tibetan plateau, Himalaya, Indian shield, and Pamir–Hindu Kush. These models approximately account for all structure with wavelength > 1000 km.

2. We found that frequency-dependent mean uncertainties in the Tibetan region phase velocity measurements are much larger than those assumed by previ-

ous authors (Figure 6). These uncertainties are for interevent phase velocity; hence, in the absence of other information, half of their value at each frequency should be used as uncertainty estimates in future work in the Tibetan region.

3. There is evidence to suggest that zones of low upper mantle velocity exist beneath the western and the eastern Tien Shan region. It is suggested that both of these regions define areas of mantle upwelling with downwelling cooler mantle between them.

4. The Tarim basin has a low-velocity upper crust, probably due to thick sediment accumulation. It also exhibits either an extremely fast uppermost mantle velocity or a very thick lithosphere.

5. A constant crustal velocity with depth was observed beneath the east central Tibetan plateau, whereas a positive velocity gradient with depth was found beneath the rest of the plateau (Figure 17). We suggest that these structures plus inefficient S_n transmission and subrecent basaltic volcanism can be explained by basaltic intrusions into the east central plateau lower crust, causing an increased crustal geothermal gradient and partial melting at the Moho.

6. A widespread low-velocity mantle layer exists within the depth range 115–185 km beneath the central and northeast plateau, but possibly not to the northwest, and probably not to the southern or far eastern plateau (Figure 17).

7. The data presented here are not consistent with the entire Indian crustal and upper mantle structure to 185 km depth underplating most of the Tibetan plateau. It is possible that India has underplated the plateau if either (1) the Indian lithospere is less than approximately 85 km thick or (2) the Indian lithospheric mantle has been advected away or altered approximately below 115 km depth beneath the Tibetan plateau.

Acknowledgments. Special thanks are extended to Philip England, Peter Molnar, Steve Roecker and to two anonymous reviewers, all of whom provided many helpful suggestions and criticisms. Thanks also to Jeannot Trampert for constructive comments on the phase velocity analysis.

References

Armijo, R., P. Tapponier, and T. Han, Late Cenozoic right-lateral strike-slip faulting across southern Tibet, *J. Geophys. Res.*, *94*, 2787–2838, 1989.

Avouac, J.-P., P. Tapponnier, M. Bai, H. You, and G. Wang, Active thrusting along the northern Tien Shan and late Cenozoic rotation of the Tarim relative to Dzungaria and Kazakhstan, *J. Geophys. Res.*, *98*(B4), 6755–6804, 1993.

Baranowski, J., J. Armbruster, L. Seeber, and P. Molnar, Focal depths and fault plane solutions of earthquakes and active tectonics of the Himalayas, *J. Geophys. Res.*, *89*, 6918–6928, 1984.

Barazangi, M., and J. Ni, Velocities and propogation characteristics of *Pn* and *Sn* beneath the Himalatan arc and Tibetan plateau: Possible evidence for underthrusting of Indian continental lithosphere beneath Tibet, *Geology*, *10*, 179–185, 1982.

Beloussov, V. V. et. al., Structure of the lithosphere beneath the deep seismic sounding profile: Tien Shan–Pamirs–Karakorum–Himalayas, *Tectonophysics*, *70*, 193–221, 1980.

Bird, P., Thermal and mechanical evolution of continental convergence zones: Zagros and Himalayas, Ph.D. thesis, Mass. Inst. of Technol., Cambridge, 1976.

Bird, P., Initiation of the intracontinental subduction in the Himalaya, *J. Geophys. Res.*, *83*, 4975–4987, 1978.

Bird, P., and M. N. Toksöz, Strong attenuation of Rayleigh waves in Tibet, *Nature*, *266*, 161–163, 1977.

Bourjot, L., and B. Romanowicz, Crust and upper mantle tomography in Tibet using surface waves, *Geophys. Res. Lett.*, *19*(9), 881–884, 1992.

Brandon, C., and B. Romanowicz, A "no-lid" zone in the central Chang-Thang platform of Tibet: Evidence from pure path phase velocity measurements of long period Rayleigh waves, *J. Geophys. Res.*, *91*(B6), 6547–6564, 1986.

Burke, K., J. F. Dewey, and W. S. F. Kidd, The Tibetan plateau; its significance for tectonics and petrology, *Geol. Soc. Am. Abstr. Programs*, *6*, 1027–1028, 1974.

Burov, E. V., M. G. Kogan, H. Lyon-Caen, and P. Molnar, Gravity anomalies, the deep structure, and dynamic processes beneath the Tien Shan, *Earth Planet. Sci. Lett.*, *96*, 367–383, 1990.

Burtman, V. S., and P. Molnar, Geological and geophysical evidence for deep subduction of continental crust beneath the Pamir, *Geol. Soc. Am. Spec. Pap.*, *281*, 1–76, 1993.

Cara, M., Filtering of dispersed wavetrains, *Geophys. J. R. Astron. Soc.*, *33*, 65–80, 1973.

Chen, W.-P., and P. Molnar, Short-period Rayleigh-wave dispersion across the Tibetan plateau, *Bull. Seismol. Soc. Am.*, *65*(5), 1051–1057, 1975.

Chen, W.-P., and P. Molnar, Constraints on the seismic wave velocity structure beneath the Tibetan plateau and their tectonic implications, *J. Geophys. Res.*, *86*(B7), 5937–5962, 1981.

Chun, K. Y., and T. V. McEvilly, Crustal structure in Tibet: High seismic velocity in the lower crust, *J. Geophys. Res.*, *91*(B10), 10,405–10,411, 1986.

Chun, K. Y., and T. Yoshii, Crustal structure of the Tibetan plateau: A surface wave study, *Bull. Seismol. Soc. Am.*, *67*, 735–750, 1977.

Curtis, A., Shear wave studies and elastic models of extensional zones: The Tibetan plateau and Aegan region, Ph.D. thesis, Dep. of Earth Sci., Univ. of Oxford, Oxford, England, 1994.

Dewey, J. F., and K. C. A. Burke, Tibetan, Variscan and Precambrian basement reactivation: products of a continental collision, *J. of Geol.*, *81*, 683–692, 1973.

Duffy, T. S., and D. L. Anderson, Seismic velocities in mantle minerals and the mineralogy of the upper mantle, *J. Geophys. Res.*, *94*, 1,895–1,912, 1989.

Dziewonski, A. M., and D. L. Anderson, Preliminary reference Earth model, *Phys. Earth Planet. Inter.*, *125*, 297–356, 1981.

Dziewonski, A. M., and J. H. Woodhouse, An experiment in systematic study of global seismicity: Centroid–moment tensor solutions for 201 moderate and large earthquakes of 1981, *J. Geophys. Res.*, *88*, 3247–3271, 1983.

Dziewonski, A. M., A. L. Hales, and E. R. Lapwood, Parametrically simple Earth models consistent with geophysical data, *Phys. Earth Planet. Inter.*, *10*, 12–48, 1975.

England, P., and G. Houseman, Finite strain calculations of continental deformation, 2, Comparison with the India–Asia collision zone, *Annu. Rev. Earth Planet. Sci.*, *17*, 197–226, 1986.

England, P., and D. McKenzie, A thin viscous sheet model

for continental deformation, *Geophys. J. R. Astron. Soc.*, *70*, 295–321, (Correction to A thin viscous sheet model for continental deformation, *Geophys. J. R. Astron. Soc.*, *73*, 523, 1983.), 1982.

Fan, G., J. F. Ni, and T. C. Wallace, Active tectonics of the Pamir and Karakorum, *J. Geophys. Res.*, *99*, 7131–7160, 1994.

Fisher, R. L., J. G. Sclater, and D. P. McKenzie, Evolution of the central Indian ridge, western Indian ocean, *Geol. Soc. Am. Bull.*, *82*, 553–562, 1971.

Gansser, A., The significance of the Himalayan suture zone, *Tectonophysics*, *62*, 37–52, 1980.

Grand, S. P., and D. V. Helmberger, Upper-mantle shear structure beneath Asia from multi-bounce *S*-waves, *Phys. Earth Planet. Inter.*, *41*, 154–169, 1985.

Gupta, H. K., and H. Narain, Crustal structure in the Himalayan and Tibet plateau region from surface wave dispersion, *Bull. Seismol. Soc. Am.*, *57*, 235–248, 1967.

Hirn, A., G. Jobert, G. Wittlinger, Z.-Y. Xu, and E.-Y. Gao, Main features of the upper lithosphere in the unit between the High Himalayas and the Yarlung Zangbo Jiang suture, *Ann. Geophys.*, *2*(2), 113–118, 1984.

Holt, W. E., and T. C. Wallace, Crustal thickness and upper mantle velocities in the Tibetan plateau region from the inversion of regional P_{nl} waveforms: Evidence for a thick upper mantle lid beneath southern Tibet, *J. Geophys. Res.*, *95*(B8), 12,499–12,525, 1990.

Huestis, S., P. Molnar, and J. Oliver, Regional S_n velocities and shear velocity in the upper mantle, *Bull. Seismol. Soc. Am.*, *63*, 469–475, 1973.

Kidd, W. S. F., Widespread late Neogene and Quaternary calc-alkaline vulcanism on the Tibetan plateau, *EOS Trans. AGU*, *56*(6), 453, 1975.

Kosarev, G. L., N. V. Petersen, L. P. Vinnik, and S. W. Roecker, Receiver functions for the Tien Shan broadband analogue network: Contrasts in the evolution of structures across the Telas–Fergana fault, *J. Geophys. Res.*, *98*, 4437–4448, 1993.

Kulagina, M. V., A. A. Lukk, and B. K. Kulagin, Block structure of the Earth's crust of Tadjikstan (in Russian), in *Searches for Precursors of Earthquakes in Prediction Polygons*, pp. 70–84. Nauka, Moscow, 1974.

Landisman, M., A. Dziewonsky, and Y. Satô, Recent improvements in the analysis of surface wave observations, *Geophys. J. R. Astron. Soc.*, *17*, 369–403, 1969.

Lepine, J.-C., A. Hirn, M. R. Pandey, and J. M. Tater, Features of the *P*-waves propagated in the crust of the Himalayas, *Ann. Geophys.*, *2*, 119–121, 1984.

Lyon-Caen, H., Comparison of the upper mantle shear wave velocity structure of the Indian Shield and the Tibetan plateau and tectonic implications, *Geophys. J. R. Astron. Soc.*, *86*, 727–749, 1986.

Lyon-Caen, H., and P. Molnar, Constraints on the structure of the Himalaya from an analysis of gravity anomalies and a flexural model of the lithosphere, *J. Geophys. Res.*, *88*(B10), 8171–8191, 1983.

Lyon-Caen, H., and P. Molnar, Gravity anomalies and the structure of western Tibet and the southern Tarim Basin, *Geophys. Res. Lett.*, *11*, 1251–1254, 1984.

Makeyeva, L. I., L. P. Vinnik, and S. W. Roecker, Shear wave splitting and small-scale convection in the continental upper mantle, *Nature*, *358*, 144–147, 1992.

McKenzie, D. P., and J. G. Sclater, The evolution of the Indian Ocean since the late Cretaceous, *Geophys. J. R. Astron. Soc.*, *24*, 437–528, 1971.

McKenzie, D. P., J. M. Roberts, and N. O. Weiss, Convection in the Earth's mantle: Towards a numerical simulation, *J. Fluid Mech.*, *62*, 465–538, 1974.

McNamara, D. E., T. J. Owens, P. G. Silver, and F. T. Wu, Shear wave anisotropy beneath the Tibetan plateau, *J. Geophys. Res.*, *99*(B7), 13,655–13,665, 1994.

McNamara, D. E., W. R. Walters, T. J. Owens, and C. J. Ammon, Upper mantle velocity structure beneath the Tibetan plateau from P_n travel time tomography, *J. Geophys. Res.*, *102*, 493–505, 1997.

Min, Z., and F. T. Wu, Nature of the upper crust beneath Tibet, *Earth Planet. Sci. Lett.*, *84*, 204–210, 1987.

Mishra, D. C., Crustal structure and dynamics under the Himalayas and Pamir ranges, *Earth Planet. Sci. Lett.*, *57*, 415–420, 1981.

Molnar, P., Structure and tectonics of the Himalaya: Constraints and implications of geophysical data, *Annu. Rev. Earth Planet. Sci.*, *12*, 489–518, 1984.

Molnar, P., A review of geophysical constraints on the deep structure of the Tibetan plateau, the Himalaya and the Karakorum, and their tectonic implications, *Philos. Trans. R. Soc. London, Ser. B*, *326*, 33–88, 1988.

Molnar, P., *S*-wave residuals from earthquakes in the Tibetan region and lateral variations in the upper mantle, *Earth Planet. Sci. Lett.*, *101*, 68–77, 1990.

Molnar, P., Crust in mantle overdrive, *Nature*, *358*, 105–106, 1992.

Molnar, P., and W.-P. Chen, *S–P* travel time residuals and lateral inhomogeneity in the mantle beneath Tibet and the Himalaya, *J. Geophys. Res.*, *89*(B8), 6911–6917, 1984.

Molnar, P., and P. Tapponnier, Cenozoic tectonics of Asia: Effects of a continental collision, *Science*, *189*(4201), 421–426, 1975.

Molnar, P., B. C. Burchfiel, Z. Ziyun, L. K'uangyi, W. Shuji, and H. Minmin, Geologic evolution of northern Tibet: Results of an expedition to Ulugh Muztagh, *Science*, *235*, 299–305, 1987.

Ni, J., and M. Barazangi, Seismotectonics of the Himalayan collision zone: Geometry of the underthrusting Indian plate beneath the Himalayas, *J. Geophys. Res.*, *89*, 1147–1163, 1984.

Patton, H., Crust and upper mantle structure of the Eurasian continent from phase velocity and *Q* of surface waves, *Rev. Geophys.*, *18*(3), 605–625, 1980.

Peltzer, G., P. Tapponnier, Y. Gaudemer, B. Meter, G. Shunmin, Y. Kelun, C. Zhitai, and D. Huagung, Offsets of late Quaternary morphology, rate of slip, and recurrence of large earthquakes on the Chang Ma fault (Gansu, China), *J. Geophys. Res.*, *93*(B7), 7793–7812, 1988.

Pettersen, O., and D. J. Doornbos, A comparison of source analysis methods as applied to earthquakes in Tibet, *Phys. Earth Planet. Inter.*, *47*, 125–136, 1987.

Pines, I., T.-L. Teng, and R. Rosenthal, A surface wave dispersion study of the crustal and upper mantle structure of China, *J. Geophys. Res.*, *85*(B7), 3829–3844, 1980.

Roecker, S. W., Velocity structure of the Pamir–Hindu Kush region: Possible evidence of subducted crust, *J. Geophys. Res.*, *87*, 945–959, 1982.

Roecker, S. W., T. M. Sabitova, L. P. Vinnik, Y. A. Burmakov, M. I. Golvanov, R. Mamatkanova, and L. Munirova, Three-dimensional elastic wave velocity structure of the western and central Tien Shan, *J. Geophys. Res.*, *98*(B9), 15779 15795, 1993.

Romanowicz, B., Constraints on the structure of the Tibetan plateau from pure path phase velocities of Love and Rayleigh waves, *J. Geophys. Res.*, *87*(B8), 6865–6883, 1982.

Sahni, A., and V. Kumar, Palaeogene palaeobiogeography of the Indian subcontinent, *Palaeogeogr. Palaeoclimatol. Palaeoccol.*, *15*, 209 226, 1974.

Sapin, M., X. J. Wang, A. Hirn, and Z. A. Xu, A seismic sounding in the crust of the Lhasa block, Tibet., *Ann. Geophys.*, pp. 637–646, 1985.

Sengör, A. M. C., and W. S. F. Kidd, Post-collisional tectonics of the Turkish- Iranian plateau and a comparison with Tibet, *Tectonophysics*, *55*, 361–376, 1979.

Shaw, P., and J. Orcutt, Propagation of P_l and implications for the structure of Tibet, *J. Geophys. Res.*, *89*, 3135–3152, 1984.

Tarantola, A., and B. Valette, Inverse problems = Quest for information, *J. Geophys.*, *50*, 159–170, 1982.

Wang, Q. M., T. Nishidai, and M. P. Coward, The Tarim Basin, NW China: Formation and aspects of petroleum geology, *J. Petrol. Geol.*, *15*(1), 5–34, 1992.

Westaway, R., Crustal volume balance during the India-Eurasia collision and altitude of the Tibetan plateau: A working hypothesis, *J. Geophys. Res.*, *100*(B8), 15,173–15,192, 1995.

Willett, S. D., and C. Beaumont, Subduction of Asian lithospheric mantle beneath Tibet inferred from models of continental collision, *Nature*, *369*, 642–645, 1994.

Zhao, L.-S., and W. J. Morgan, Uplift of Tibetan plateau, *Tectonics*, *4*(4), 359–369, 1985.

Zhao, L.-S., and W. J. Morgan, Injection of Indian crust into Tibetan lower crust: A two-dimensional finite element model study, *Tectonics*, *6*(4), 489–504, 1987.

Zhao, L.-S., and J. Xie, Lateral variations in compressional velocities beneath the Tibetan plateau from Pn traveltime tomography, *Geophys. J. Int.*, *115*, 1,070–1,084, 1993.

Zhao, L.-S., D. V. Helmberger, and D. G. Harkrider, Shear-velocity structure of the crust and upper mantle beneath the Tibetan plateau and southeastern China, *Geophys. J. Int.*, *105*, 713–730, 1991.

Zhao, L.-S., A. Hasegawa, and S. Hirouchi, Tomographic imaging of P and S wave velocity structure beneath northeastern Japan, *J. Geophys. Res.*, *97*, 19,909–19,928, 1992.

A. Curtis, Department of Theoretical Geophysics, Faculteit Aardwetenschappen, Budapestlaan 4, Postbus 80.021, 3508 TA Utrecht, The Netherlands. (email: curtis@geof.ruu.nl)

J. H. Woodhouse, Department of Earth Sciences, Oxford University, Parks Road, Oxford OX2 6HG, England.

(Received November 28, 1995; revised September 23, 1996; accepted October 11, 1996.)